A&A 557, A52 (2013)
DOI: 10.1051/0004-6361/201220941

Astronomy & Astrophysics

Planck intermediate results

XI. The gas content of dark matter halos: the Sunyaev-Zeldovich-stellar mass relation for locally brightest galaxies

Planck Collaboration: P. A. R. Ade[82], N. Aghanim[57], M. Arnaud[71], M. Ashdown[68,7], F. Atrio-Barandela[19], J. Aumont[57], C. Baccigalupi[81], A. Balbi[36], A. J. Banday[90,10], R. B. Barreiro[65], R. Barrena[64], J. G. Bartlett[1,66], E. Battaner[92], K. Benabed[58,88], J.-P. Bernard[10], M. Bersanelli[34,50], I. Bikmaev[21,3], J. J. Bock[66,11], H. Böhringer[76], A. Bonaldi[67], J. R. Bond[9], J. Borrill[14,84], F. R. Bouchet[58,88], H. Bourdin[36], R. Burenin[83], C. Burigana[49,32], R. C. Butler[49], P. Cabella[37], A. Chamballu[71,16,57], R.-R. Chary[55], L.-Y Chiang[61], G. Chon[76], P. R. Christensen[78,38], D. L. Clements[54], S. Colafrancesco[46], S. Colombi[58,88], L. P. L. Colombo[25,66], B. Comis[72], A. Coulais[70], B. P. Crill[66,79], F. Cuttaia[49], A. Da Silva[12], H. Dahle[63], R. J. Davis[67], P. de Bernardis[33], G. de Gasperis[36], A. de Rosa[49], G. de Zotti[45,81], J. Delabrouille[1], J. Démoclès[71], J. M. Diego[65], H. Dole[57,56], S. Donzelli[50], O. Doré[66,11], M. Douspis[57], X. Dupac[41], G. Efstathiou[62], T. A. Enßlin[75], F. Finelli[49,51], I. Flores-Cacho[10,90], O. Forni[90,10], M. Frailis[47], E. Franceschi[49], M. Frommert[18], S. Galeotta[47], K. Ganga[1], R. T. Génova-Santos[64], M. Giard[90,10], Y. Giraud-Héraud[1], J. González-Nuevo[65,81], K. M. Górski[66,94], A. Gregorio[35,47], A. Gruppuso[49], F. K. Hansen[63], D. Harrison[62,68], C. Hernández-Monteagudo[13,75], D. Herranz[65], S. R. Hildebrandt[11], E. Hivon[58,88], M. Hobson[7], W. A. Holmes[66], A. Hornstrup[17], W. Hovest[75], K. M. Huffenberger[93], G. Hurier[72], T. R. Jaffe[90,10], A. H. Jaffe[54], W. C. Jones[27], M. Juvela[26], E. Keihänen[26], R. Keskitalo[23,14], I. Khamitov[87,21], T. S. Kisner[74], R. Kneissl[40,8], J. Knoche[75], M. Kunz[18,57,4], H. Kurki-Suonio[26,44], A. Lähteenmäki[2,44], J.-M. Lamarre[70], A. Lasenby[7,68], C. R. Lawrence[66], M. Le Jeune[1], R. Leonardi[41], P. B. Lilje[63], M. Linden-Vørnle[17], M. López-Caniego[65], P. M. Lubin[29], G. Luzzi[69], J. F. Macías-Pérez[72], C. J. MacTavish[68], B. Maffei[67], D. Maino[34,50], N. Mandolesi[49,6,32], M. Maris[47], F. Marleau[60], D. J. Marshall[71], E. Martínez-González[65], S. Masi[33], M. Massardi[48], S. Matarrese[31], P. Mazzotta[36], S. Mei[43,89,11], A. Melchiorri[33,52], J.-B. Melin[16], L. Mendes[41], A. Mennella[34,50], S. Mitra[53,66], M.-A. Miville-Deschênes[57,9], A. Moneti[58], L. Montier[90,10], G. Morgante[49], D. Mortlock[54], D. Munshi[82], J. A. Murphy[77], P. Naselsky[78,38], F. Nati[33], P. Natoli[32,5,49], H. U. Nørgaard-Nielsen[17], F. Noviello[67], D. Novikov[54], I. Novikov[78], S. Osborne[86], C. A. Oxborrow[17], F. Pajot[57], D. Paoletti[49,51], L. Perotto[72], F. Perrotta[81], F. Piacentini[33], M. Piat[1], E. Pierpaoli[25], R. Piffaretti[71,16], S. Plaszczynski[69], E. Pointecouteau[90,10], G. Polenta[5,46], L. Popa[59], T. Poutanen[44,26,2], G. W. Pratt[71], S. Prunet[58,88], J.-L. Puget[57], J. P. Rachen[22,75], R. Rebolo[64,15,39], M. Reinecke[75], M. Remazeilles[57,1], C. Renault[72], S. Ricciardi[49], I. Ristorcelli[90,10], G. Rocha[66,11], M. Roman[1], C. Rosset[1], M. Rossetti[34,50], J. A. Rubiño-Martín[64,39,⋆], B. Rusholme[55], M. Sandri[49], G. Savini[80], D. Scott[24], L. Spencer[82], J.-L. Starck[71], V. Stolyarov[7,68,85], R. Sudiwala[82], R. Sunyaev[75,83], D. Sutton[62,68], A.-S. Suur-Uski[26,44], J.-F. Sygnet[58], J. A. Tauber[42], L. Terenzi[49], L. Toffolatti[20,65], M. Tomasi[50], M. Tristram[69], L. Valenziano[49], B. Van Tent[73], P. Vielva[65], F. Villa[49], N. Vittorio[36], L. A. Wade[66], B. D. Wandelt[58,88,30], W. Wang[75], N. Welikala[57], J. Weller[91], S. D. M. White[75], M. White[28], D. Yvon[16], A. Zacchei[47], and A. Zonca[29]

(Affiliations can be found after the references)

Received 17 December 2012 / Accepted 25 June 2013

ABSTRACT

We present the scaling relation between Sunyaev-Zeldovich (SZ) signal and stellar mass for almost 260,000 locally brightest galaxies (LBGs) selected from the Sloan Digital Sky Survey (SDSS). These are predominantly the central galaxies of their dark matter halos. We calibrate the stellar-to-halo mass conversion using realistic mock catalogues based on the Millennium Simulation. Applying a multi-frequency matched filter to the *Planck* data for each LBG, and averaging the results in bins of stellar mass, we measure the mean SZ signal down to $M_* \sim 2 \times 10^{11}\ M_\odot$, with a clear indication of signal at even lower stellar mass. We derive the scaling relation between SZ signal and halo mass by assigning halo properties from our mock catalogues to the real LBGs and simulating the *Planck* observation process. This relation shows no evidence for deviation from a power law over a halo mass range extending from rich clusters down to $M_{500} \sim 2 \times 10^{13}\ M_\odot$, and there is a clear indication of signal down to $M_{500} \sim 4 \times 10^{12}\ M_\odot$. *Planck*'s SZ detections in such low-mass halos imply that about a quarter of all baryons have now been seen in the form of hot halo gas, and that this gas must be less concentrated than the dark matter in such halos in order to remain consistent with X-ray observations. At the high-mass end, the measured SZ signal is 20 % lower than found from observations of X-ray clusters, a difference consistent with the magnitude of Malmquist bias effects that were previously estimated for the X-ray sample.

Key words. cosmology: observations – cosmic background radiation – large-scale structure of Universe – galaxies: clusters: general

⋆ Corresponding author: J. A. Rubiño-Martín (e-mail: jalberto@iac.es)

1. Introduction

Galaxy evolution is currently understood to reflect a thermal cycle operating between baryonic components confined in dark matter halos. Gas cools radiatively during the hierarchical build-up of the halo population and condenses to form galaxies in halo cores. Left unchecked, cooling results in more massive galaxies than observed (Balogh et al. 2001; Lin & Mohr 2004; Tornatore et al. 2003), and one must invoke an additional source of non-gravitational heating to prevent a "cooling crisis" (White & Rees 1978; Cole 1991; White & Frenk 1991; Blanchard et al. 1992). Feedback from star formation and supernovae appears insufficient to halt cooling in massive halos (Borgani et al. 2004), so some modelers have invoked additional heating by active galactic nuclei (AGN, Churazov et al. 2002; Springel et al. 2005a; McNamara & Nulsen 2007). Such models show substantially improved agreement with the luminosity-temperature relation of X-ray clusters (Valageas & Silk 1999; Bower et al. 2001; Cavaliere et al. 2002) and the luminosity function of galaxies (Croton et al. 2006; Bower et al. 2006; Somerville et al. 2008). The energetics of AGN feedback imply that it should have especially strong effects on low-mass clusters, heating gas in the central regions and pushing it to larger radii, thereby reducing both gas fractions and X-ray luminosities (Puchwein et al. 2008; McCarthy et al. 2010).

Relationships between the gas, stellar, and dark matter properties of halos are important to our understanding of galaxy formation. Measurements of these relationships over a wide range of halo mass, from rich clusters down to individual galaxies, are therefore a primary objective of a number of current observational campaigns. Recent studies have probed the relationship between the mass of a halo and the stellar mass of its central galaxy (the SHM relation) using "abundance matching" techniques, the dynamics of satellite galaxy populations, and gravitational lensing (Guo et al. 2010; Moster et al. 2010; Mandelbaum et al. 2006; Leauthaud et al. 2012).

Corresponding constraints on the gas content of halos over a similar mass range are not yet available. Although there are many detailed X-ray studies of the intracluster medium, these mostly concern massive clusters; lower mass groups are faint and so are difficult to study individually. The Sunyaev-Zeldovich (SZ) effect (Sunyaev & Zeldovich 1972; Birkinshaw 1999) offers a fresh means to address this problem. Large-area SZ surveys are just beginning to be amassed by ground-based instruments such as the Atacama Cosmology Telescope (ACT, Swetz et al. 2008; Marriage et al. 2011; Sehgal et al. 2011; Hand et al. 2011), the South Pole Telescope (SPT, Carlstrom et al. 2011; Staniszewski et al. 2009; Vanderlinde et al. 2010; Williamson et al. 2011) and APEX-SZ (Dobbs et al. 2006), as well as by the *Planck*[1] satellite mission, (Planck Collaboration 2011c,d,e,f,g).

High signal-to-noise ratio observations of individual objects are not currently possible over the full mass range from galaxy clusters down to individual bright galaxies. The SHM relation can only be estimated for lower mass objects through statistical methods applied to large catalogues. In this context, the SZ effect presents exciting new opportunities. First steps in this direction were taken by Planck Collaboration (2011g) and Hand et al. (2011), with more recent work by Draper et al. (2012) and Sehgal et al. (2013). In our first study (Planck Collaboration 2011g), we binned large numbers of maxBCG (Koester et al. 2007) clusters by richness to measure the relation between mean SZ signal and richness. In a similar manner, Hand et al. (2011) binned ACT measurements of luminous red galaxies to determine the mean relation between SZ signal and LRG luminosity.

Here, we extend our previous work with *Planck* multi-frequency observations of a large sample of locally brightest galaxies (LBGs). These were selected from the Sloan Digital Sky Survey (SDSS) using criteria designed to maximize the fraction of objects that are the central galaxies of their dark matter halos. We stack the *Planck* data in order to estimate the mean SZ signal for LBGs in a series of stellar mass bins. We then use mock galaxy catalogues based on the Millennium Simulation and tuned to fit the observed abundance and clustering of SDSS galaxies to establish the relation between stellar and halo mass. *Planck* is a unique SZ instrument for this purpose because of its large frequency coverage and the fact that it observes the entire SDSS survey area, allowing study of large samples of galaxy systems with extensive multi-wavelength data.

We unambiguously ($>3\sigma$) detect the SZ signal down to stellar masses of $2 \times 10^{11}\ M_\odot$, corresponding to an effective halo mass M_{500} of $2 \times 10^{13}\ M_\odot$ (see Sect. 2) and we find clear indications of signal down to $10^{11}\ M_\odot$ ($M_{500} = 4 \times 10^{12}\ M_\odot$). Detailed simulation both of the galaxy sample and of the *Planck* measurement process allows us to correct the effects of halo miscentering and of the scatter in halo mass at fixed stellar mass when estimating the SZ signal-halo mass relation. We find that the relation is well described by a single power law within its statistical uncertainties. At the high end, our results overlap the mass range probed by X-ray clusters, where we find a 20% lower SZ signal than obtained from fits to X-ray selected cluster samples. This difference is consistent with possible Malmquist bias effects in the X-ray sample. The gas properties of dark matter halos display a remarkable regularity from the poorest groups to the richest clusters.

Throughout this paper, we adopt a fiducial ΛCDM cosmology consistent with the WMAP7 results (Komatsu et al. 2011). In particular, we use $\Omega_\mathrm{m} = 0.272$, $\Omega_\Lambda = 0.728$, $n_\mathrm{s} = 0.961$, and $\sigma_8 = 0.807$. We express the Hubble parameter at redshift z as $H(z) = H_0 E(z)$, with $H_0 = h \times 100\,\mathrm{km\,s^{-1}\,Mpc^{-1}}$ and $h = 0.704$. For the redshift range of interest ($z \lesssim 1$), we approximate $E^2(z) = \Omega_\mathrm{m}(1+z)^3 + \Omega_\Lambda$. The virial radius of a halo is defined here as R_{200}, the radius enclosing a mean density 200 times the critical density at that redshift, i.e., $200 \times \rho_\mathrm{c}(z)$, where $\rho_\mathrm{c}(z) = 3H^2(z)/(8\pi G)$. The virial mass is then defined as

$$M_{200} \equiv 200(4\pi/3)R_{200}^3 \rho_\mathrm{c},$$

which we also refer to as M_h. Similarly, we quote the conventional masses M_{500} and radii, R_{500}, when presenting the SZ scalings. For stellar mass, we use the symbol M_*.

The SZ signal is characterized by Y_{500}, the Comptonization parameter integrated over a sphere of radius R_{500}, expressed in square arcminutes. Specifically,

$$Y_{500} \equiv (\sigma_\mathrm{T}/(m_\mathrm{e}c^2)) \int_0^{R_{500}} P \mathrm{d}V / D_\mathrm{A}^2(z),$$

where $D_\mathrm{A}(z)$ is the angular-diameter distance, σ_T is the Thomson cross-section, c is the speed of light, m_e is the electron rest mass, and $P = n_\mathrm{e} k T_\mathrm{e}$ is the pressure, obtained as the product of the electron number density and the electron temperature. Throughout this paper, we use the quantity

$$\tilde{Y}_{500} \equiv Y_{500} E^{-2/3}(z) (D_\mathrm{A}(z)/500\ \mathrm{Mpc})^2,$$

[1] *Planck* (http://www.esa.int/Planck) is a project of the European Space Agency (ESA) with instruments provided by two scientific consortia funded by ESA member states (in particular the lead countries France and Italy), with contributions from NASA (USA) and telescope reflectors provided by a collaboration between ESA and a scientific consortium led and funded by Denmark.

also expressed in square arcminutes, as the intrinsic SZ signal, scaled to redshift $z = 0$ and to a fixed angular diameter distance.

The paper is organized as follows. Section 2 describes the *Planck* maps used in our analysis, and our reference catalogue of locally brightest galaxies, based on SDSS data. Section 3 describes our methodology. Sections 4 and 5 gives our main results and the tests made to demonstrate their robustness. Sections 6 and 7 contain discussion and conclusions, respectively.

2. Data

2.1. Planck data set

Planck (Tauber et al. 2010; Planck Collaboration 2011a) is the third generation space mission to measure the anisotropy of the cosmic microwave background (CMB). It observes the sky in nine frequency bands covering 30–857 GHz with high sensitivity and angular resolution from 31′ to 5′. The Low Frequency Instrument (LFI; Mandolesi et al. 2010; Bersanelli et al. 2010; Mennella et al. 2011) covers the 30, 44, and 70 GHz bands with amplifiers cooled to 20 K. The High Frequency Instrument (HFI; Lamarre et al. 2010; Planck HFI Core Team 2011a) covers the 100, 143, 217, 353, 545, and 857 GHz bands with bolometers cooled to 0.1 K. Polarisation is measured in all but the highest two bands (Leahy et al. 2010; Rosset et al. 2010). A combination of radiative cooling and three mechanical coolers produces the temperatures needed for the detectors and optics (Planck Collaboration 2011b). Two data processing centres (DPCs) check and calibrate the data and make maps of the sky (Planck HFI Core Team 2011b; Zacchei et al. 2011). *Planck*'s sensitivity, angular resolution, and frequency coverage make it a powerful instrument for Galactic and extragalactic astrophysics as well as for cosmology. Early astrophysics results are given in Planck Collaboration VIII–XXVI 2011, based on data taken between 13 August 2009 and 7 June 2010. Intermediate astrophysics results are now being presented in a series of papers based on data taken between 13 August 2009 and 27 November 2010.

2.2. A locally brightest galaxy catalogue

To select a sample of central galaxies, we first define a parent population with $r < 17.7$ (r-band, extinction-corrected, Petrosian magnitude) from the spectroscopic galaxy catalogue of the New York University Value Added Galaxy Catalogue[2]. This was built by Blanton et al. (2005) based on the seventh data release of the Sloan Digital Sky Survey (SDSS/DR7 Abazajian et al. 2009). This parent catalogue contains 602 251 galaxies. We then define "locally brightest galaxies" to be the set of all galaxies with $z > 0.03$ that are brighter in r than all other sample galaxies projected within 1.0 Mpc and with redshift differing by less than 1000 km s^{-1}. After this cut 347 486 locally brightest galaxies remain.

The SDSS spectroscopic sample is incomplete because it proved impossible to place a fibre on every object satisfying the photometric selection criteria, and because some spectra failed to give acceptable redshifts. The completeness to our chosen magnitude limit varies with position, with a mean of 91.5% over the survey as a whole. To ensure that galaxies without SDSS spectroscopy do not violate our sample selection criteria, we have used SDSS photometry to eliminate all objects with a companion that is close and bright enough that it might violate the above criteria. Specifically, we have used the "photometric redshift 2" catalogue (photoz2 Cunha et al. 2009) from the SDSS DR7 website to search for additional companions. This catalogue tabulates a redshift probability distribution in bins of width $\Delta z = 0.0145$ for every galaxy down to photometric limits much fainter than we require. We then eliminate any candidate with a companion in this catalogue of equal or brighter r-magnitude and projected within 1.0 Mpc, unless the photometric redshift distribution of the "companion" is inconsistent with the spectroscopic redshift of the candidate. (Our definition of "inconsistent" is that the total probability for the companion to have a redshift equal to or less than that of the candidate is less than 0.1; in practice this eliminates "companions" that are too red to be at a redshift as low as that of the candidate.) This procedure leaves us with a cleaned sample of 259 579 locally brightest galaxies.

The NYU-VAGC provides a variety of data for each galaxy. In addition to the positions, magnitudes, and redshifts used to create our sample, we will make use of rest-frame colours and stellar masses. The latter are based on stellar population fits to the five-band SDSS photometry and on the measured redshifts, assuming a Chabrier (2003) stellar initial mass function (Blanton & Roweis 2007). The estimated (statistical) error in these stellar masses, arising from photometric uncertainties and template mismatches, is ∼0.1 dex. In Fig. 1 we compare the colour and redshift distributions of our final sample of locally brightest galaxies to those of the parent sample for five disjoint ranges of stellar mass. For $\log_{10} M_*/M_\odot \geq 10.8$, the distributions are similar for the two populations. At lower stellar mass, locally brightest galaxies are a small fraction of the parent sample and are biased to bluer colours and to slightly larger redshifts. In our stacking analysis below, we obtain significant SZ signals only for galaxies with $\log_{10} M_*/M_\odot \geq 11.0$. Our sample contains 81 392 galaxies satisfying this bound, the great majority of them on or near the red sequence.

2.2.1. The reliability of our central galaxy sample and its stellar mass-halo mass relation

We expect the majority of our locally brightest galaxies to be the central galaxies of their dark matter halos, just as bright field galaxies lie at the centres of their satellite systems and cD galaxies lie near the centres of their clusters and are normally their brightest galaxies. For our later analysis, it is important to know both the reliability of our galaxy sample, i.e., the fraction of galaxies that are indeed the central galaxies of their halos, and the relation between the observable stellar masses of the galaxies and the unobservable masses of their halos. In this section we investigate both issues using an update of the publicly available[3] semi-analytic galaxy formation simulation of Guo et al. (2011). The update uses the technique of Angulo & White (2010) to rescale the Millennium Simulation (Springel et al. 2005b) to the WMAP7 cosmology, then readjusts the galaxy formation parameters to produce a $z = 0$ galaxy population with abundance and clustering properties that are almost indistinguishable from those of the original model. At the relatively high masses relevant for our work, this simulation provides a very close match to the observed luminosity and stellar mass functions of the SDSS as well as to the auto-correlations of SDSS galaxies as a function of stellar mass (Guo et al. 2013).

We construct a sample of locally brightest galaxies from this simulation using criteria exactly analogous to those used for the measured data. We project the galaxy distribution onto one of

[2] NYU-VAGC, http://sdss.physics.nyu.edu/vagc/

[3] http://www.mpa-garching.mpg.de/millennium

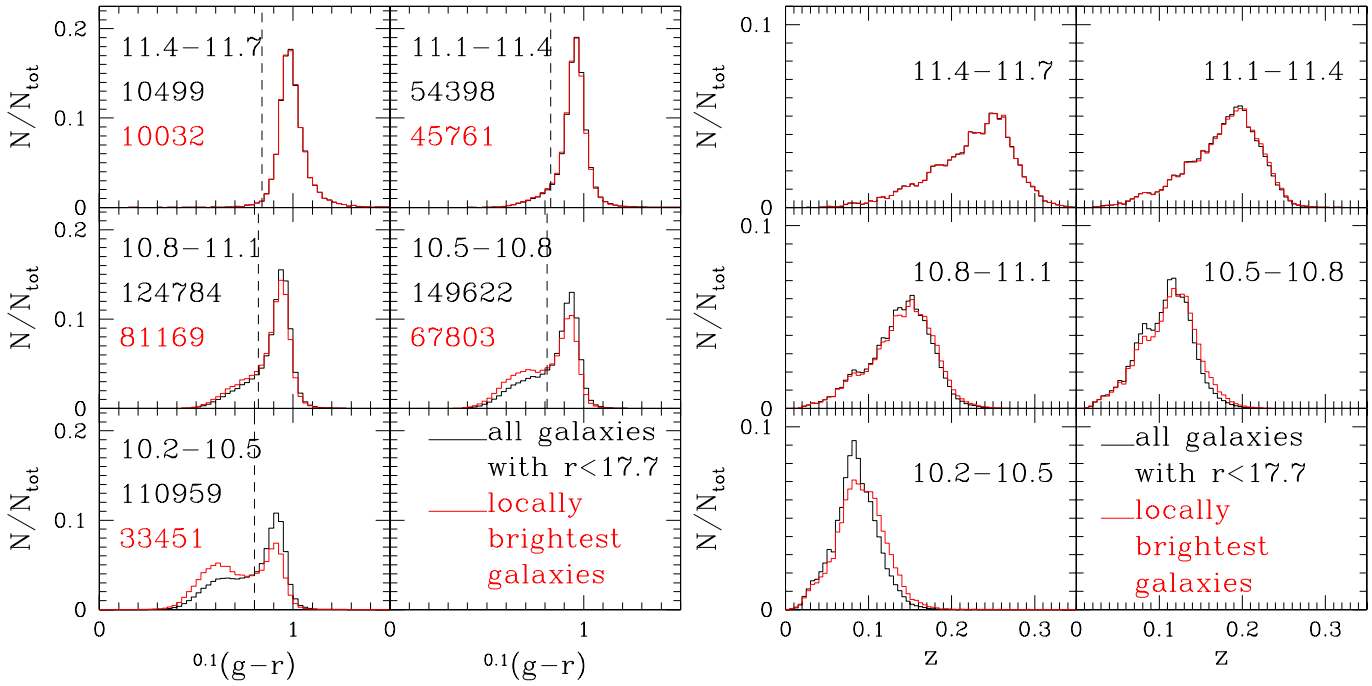

Fig. 1. Distributions in colour (*left*) and redshift (*right*) of our locally brightest galaxies and of the SDSS/DR7 population from which they were drawn. Black histograms refer to the parent sample and red histograms to the locally brightest galaxies. The panels in each set correspond to five disjoint ranges of $\log_{10} M_*/M_\odot$, as indicated in the labels. In the left-hand set, additional labels give the number of galaxies contributing to the parent (black) and locally brightest (red) histograms. Dashed vertical lines in these same panels indicate the colour we use to separate red and blue galaxies in Fig. 3 below.

the faces of the simulation cube and assign each galaxy a redshift based on its distance and peculiar velocity in the projection direction. A galaxy is considered locally brightest if it has no neighbour that is brighter in r within 1.0 Mpc projected distance and 1000 km s^{-1} in redshift. We divide galaxies into "centrals", defined as those lying at the minimum of the gravitational potential of the dark matter friends-of-friends (FoF) group with which they are associated, and "satellites", defined as all other galaxies.

With these definitions we can assess the fraction of our locally brightest galaxies that are truly central galaxies. The black line in Fig. 2 shows, as a function of stellar mass, the fraction of *all* galaxies in the simulation that are centrals. At stellar masses just above $10^{10}\,M_\odot$ this fraction is about one half, but it increases with stellar mass, reaching two thirds by $\log_{10} M_*/M_\odot = 11.0$ and 90% by $\log_{10} M_*/M_\odot = 11.8$. In contrast, the fraction of locally brightest galaxies that are centrals is much higher, with a minimum of just over 83% at stellar masses somewhat above $10^{11}\,M_\odot$. We have checked those locally brightest galaxies that are satellites, finding that for $\log_{10} M_*/M_\odot > 11$, about two-thirds are brighter than the true central galaxies of their halos. The remainder are fainter than their centrals, and are considered locally brightest because they are more than 1 Mpc (projected) from their centrals (60%) or have redshifts differing by more than 1000 km s^{-1} (40%).

We can assign a halo mass, M_{200}, to every galaxy in our simulation. For both satellite galaxies and central galaxies, we take M_{200} to be the current M_{200} of the FoF dark matter halo with which the object is associated, i.e., the mass contained within its R_{200}. Figure 3 shows a scatter plot of M_{200} against M_* for a random subset (one out of every 80) of our sample of simulated locally brightest galaxies. We indicate central galaxies with red or blue points according to their rest-frame $g - r$ colour (with the two distinct regions separated by the vertical dashed lines in the left panel of Fig. 1) while satellite galaxies are indicated by

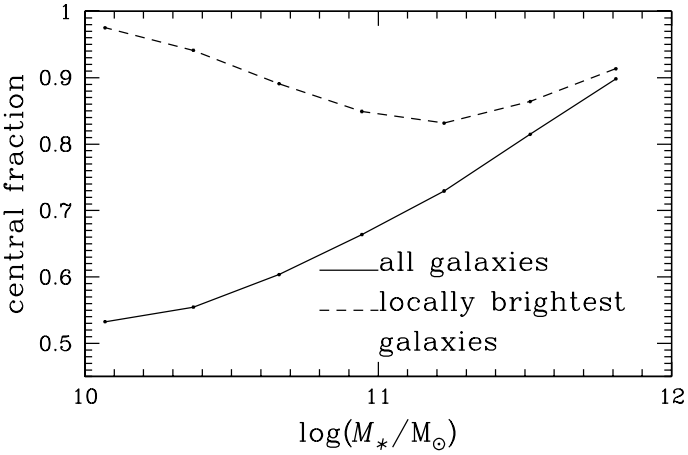

Fig. 2. Fraction of locally brightest galaxies that are the central objects in their dark halos, based on the simulations of Guo et al. (2011). The solid line traces the fraction of *all* simulated galaxies that are central galaxies as a function of stellar mass. This fraction increases with stellar mass, reaching 90% at the high mass end. The dashed line presents the central galaxy fraction for locally brightest galaxies selected from the simulation according to the criteria applied to the SDSS data. This yields a sample that is over 83% reliable at all stellar masses.

black points. Clearly, red (passive) and blue (star-forming) central galaxies lie on different M_{200}-M_* relations. That for passive galaxies is steeper, and is offset to larger halo mass in the stellar mass range where both types of central galaxy are present.

Satellite galaxies lie in halos in the massive tail of the distribution for central galaxies of the same stellar mass. Satellites misidentified as centrals in our catalogue are usually outlying members projected at relatively large separation (from a few hundred kiloparsecs to 2 Mpc). Their presence bias high both the

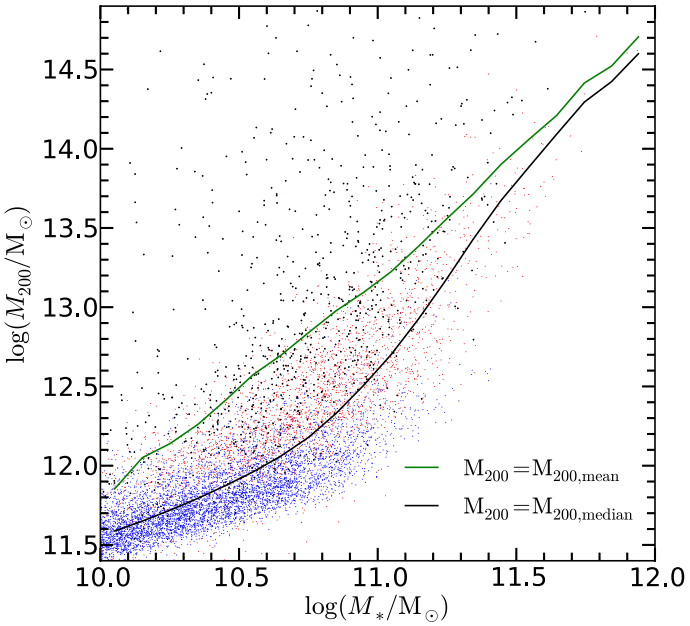

Fig. 3. Scatter plot of M_{200} against M_* for a random subset (one out of 80) of our sample of simulated locally brightest galaxies. Central galaxies are shown as red or blue points according to their $g - r$ colour, using the cuts indicated in Fig. 1. Satellite galaxies are shown as black points. The lower and upper curves give the median and mean values of halo mass as a function of stellar mass.

mean halo mass (the high black points in Fig. 3) and the spatial extent of the stacked SZ signals we measure below. However, since two thirds of the satellites that we misidentify as central galaxies are in fact brighter than the true central galaxies of their halos (i.e., they are not typical satellites), this bias is not extreme. In any case, we correct for these effects explicitly in our analysis using the simulation.

The lower of the two continuous curves in Fig. 3 shows the median M_{200} as a function of M_*. We will take this as an estimate of the typical halo mass associated with a central galaxy of known M_*, and will use it to set the angular size of the matched filter for each observed galaxy when stacking SZ signal as a function of stellar mass. The upper continuous curve shows the mean M_{200} as a function of M_*. The substantial shift between the two is a measure of the skewness induced by the differing relations for passive and star-forming centrals and by the presence of the tail of cluster satellite galaxies (see Appendix B).

3. Analysis

Our analysis closely follows that presented in Planck Collaboration (2011e), Planck Collaboration (2011f), and Planck Collaboration (2011g), employing as primary method a multi-frequency matched filter (MMF) optimized in both frequency and angular space to extract the thermal SZ signal (Herranz et al. 2002; Melin et al. 2006). We find that dust emission from our target sources affects the MMF measurements noticeably at low stellar mass, and that an effective mitigation is to restrict our final measurements to the three lowest HFI frequencies (100, 143, and 217 GHz). This is detailed in Sect. 5. Our primary scientific results are hence all based on this three-band MMF.

For the SZ model template, we employ, as in earlier work (Planck Collaboration 2011e,f,g), the so-called "universal pressure profile" (Arnaud et al. 2010) deduced from X-ray observations of the REXCESS cluster sample (Böhringer et al. 2007). For an easier comparison with the X-ray results, our scaling relations will be presented in terms of M_{500}. The R_{500} value associated with the halo of each central galaxy is obtained as follows. We first use the SHM relation giving the median halo M_{200} as a function of central galaxy stellar mass, as presented in Sect. 2.2.1. Then, using an NFW profile (Navarro et al. 1997) and the concentration parameter c_{200} given by Neto et al. (2007), we convert M_{200} to M_{500} and derive R_{500} for each halo. The angular scale for the filter is finally given by projecting R_{500} at the redshift of the target LBG. We have checked that different choices of the concentration parameter (see e.g. Duffy et al. 2008) produce changes on M_{500} at the level of few percent, within our modeling uncertainty.

In addition to the MMF, and in order to test the robustness of the results, the impact of foreground contamination and possible systematic effects, we have also implemented aperture photometry (hereafter AP). For the AP, given an object of certain angular size R, the method evaluates the mean temperature in a circle of radius $r = R$ and subtracts from it the average found in a surrounding ring of inner and outer radii $r = R$ and $r = fR$, respectively, with $f > 1$ (see e.g., Hernández-Monteagudo & Rubiño-Martín 2004). By removing the mean temperature in the outer region, the method corrects for large-scale fluctuations in the background. Once the temperature estimates are derived for each frequency map, they are combined with inverse-variance weighting to derive an SZ signal estimate by using the known frequency dependence of the (non-relativistic) thermal SZ effect. Our choice for the two parameters of the AP method is $(R, f) = (\mathrm{FWHM}, \sqrt{2})$. Note that the FWHM varies from one frequency band to another. We also note that the flux estimates within the aperture have to be corrected separately at each frequency by an appropriate factor in order to obtain the total flux of the source. For example, if the objects are unresolved and we assume Gaussian beams, then this correction factor is $(1 + \exp(-8\ln 2) - \exp(-4\ln 2))^{-1}$ for the above choice of R and f. For extended objects (e.g., those objects with R_{500} larger than the beam size, and which are modeled here using the "universal pressure profile"), the conversion factor can be evaluated numerically.

Using one of these methods (MMF or AP), we obtain a measure of the intrinsic SZ signal strength $\tilde{Y}_{500}(i)$ and the associated measurement uncertainty $\tilde{\sigma}_{\theta_{500}}(i)$ for the halo of each galaxy i. The majority of these individual SZ measurements have low signal-to-noise ratio. Following the approach in Planck Collaboration (2011e) and Planck Collaboration (2011g), we bin them by stellar mass, calculating the bin-average signal $\langle \tilde{Y}_{500} \rangle_b = [\sum 1/\tilde{\sigma}^2_{\theta_{500}}(i)]^{-1} \sum_{i=1}^{N_b} \tilde{Y}_{500}(i)/\tilde{\sigma}^2_{\theta_{500}}(i)$, with uncertainty $\sigma_b^{-2} = \sum_{i=1}^{N_b} 1/\tilde{\sigma}^2_{\theta_{500}}(i)$, where N_b is the number of galaxies in bin b.

4. Results

Our main observational result is given in Fig. 4 and Table 1, showing the mean SZ signal measured using the three-band MMF for locally brightest galaxies binned according to stellar mass. In the plot, the thick error bars show the uncertainty propagated from the individual measurement errors as described above, while the thin bars with large terminators give the variance of the weighted bin-average signal found by a bootstrap resampling. For the latter, we constructed 1,000 bootstrap realizations of the original LBG catalogue and performed the full analysis on each.

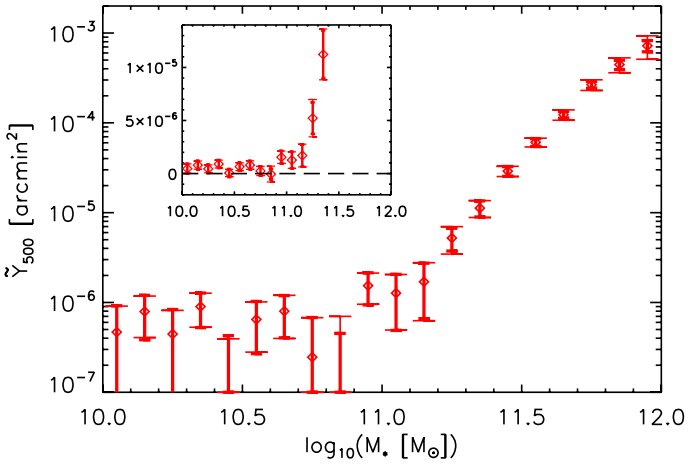

Fig. 4. Mean SZ signal vs. stellar mass for locally brightest galaxies. Thick error bars trace the uncertainty on the bin average due purely to measurement error, while thin bars with large terminators show the variance calculated by bootstrap resampling and so also include the intrinsic scatter in the signal. The inset provides a view on a linear scale to better evaluate the significance of the detections. We observe a clear relation between the mean SZ signal and stellar mass down to $\log_{10}(M_*/M_\odot) = 11.25$ (the detection in this bin is at 3.5σ), with a suggestion of signal to lower mass: the next three bins show signal at 1.6σ, 1.6σ and 2.6σ, respectively.

Table 1. *Planck* SZ signal measurements $\tilde{Y}_{500}$ binned by stellar mass (adopting a WMAP7 cosmology). These data are displayed in Fig. 4.

$\log_{10}\left(\frac{M_*}{M_\odot}\right)$	$\tilde{Y}_{500}$ [10^{-6} arcm^2]	Errors [10^{-6} arcm^2]	
		Statistical	Bootstrap
10.05	0.47	±0.45	±0.44
10.15	0.79	±0.41	±0.39
10.25	0.44	±0.39	±0.37
10.35	0.90	±0.37	±0.37
10.45	0.05	±0.37	±0.34
10.55	0.65	±0.38	±0.37
10.65	0.80	±0.39	±0.40
10.75	0.25	±0.43	±0.43
10.85	−0.05	±0.50	±0.75
10.95	1.54	±0.60	±0.58
11.05	1.27	±0.78	±0.78
11.15	1.7	±1.0	±1.1
11.25	5.2	±1.5	±1.8
11.35	11.2	±2.3	±2.4
11.45	29.0	±3.6	±3.8
11.55	60.7	±6.2	±6.8
11.65	123	±11	±16
11.75	266	±23	±36
11.85	445	±53	±84
11.95	721	±103	±210

The inset uses a linear scale to better display the significance of our detections. We have a clear signal down to the bin at $11.2 < \log_{10}(M_*/M_\odot) < 11.3$, centred at $M_* = 1.8 \times 10^{11}\ M_\odot$. The next three bins provide evidence that the signal continues to lower mass with "detections" significant at the 1.6σ, 1.6σ and 2.6σ levels, from high to low mass, respectively. The last bin is centered at $M_* = 9 \times 10^{10}\ M_\odot$, corresponding to a mean halo mass of $M_{200} \sim 1.4 \times 10^{13}\ M_\odot$. These last three bins, however, are more seriously affected by dust contamination, as discussed below, and for this reason may be more uncertain than these statistical measures suggest.

5. Systematic errors

In this section, we present a number of tests of the robustness of our principal result against systematic error. In the following, unless otherwise stated, all results use data at 100, 143, and 217 GHz only.

5.1. Stacking real-space reconstructed SZ maps

According to Fig. 4, the lowest bin at which we have a $>3\sigma$ detection is the one at $\log_{10}(M_*/M_\odot) = 11.25$. As a consistency check, and also as an illustration of the frequency dependence of the detected SZ signal, Fig. 5 shows stacked images of central galaxies in six different mass bins of width $\Delta \log_{10} M_* = 0.2$ centred at $\log_{10}(M_*/M_\odot) = 11.05, 11.15, 11.25, 11.35, 11.45$, and 11.55.

The stacked maps are obtained, using equal weights, from a (full-sky) SZ map constructed from the *Planck* 100, 143, 217, and 353 GHz maps using a modified internal linear combination algorithm (MILCA, Hurier et al. 2013) that has been used for other *Planck* Intermediate Papers (e.g., Planck Collaboration 2012a,b). The well-known internal linear combination approach (e.g., Eriksen et al. 2004) searches for the linear combination of the input maps that minimises the variance of the final reconstructed map while imposing spectral constraints. This preserves the thermal SZ signal and removes the CMB contamination (using the known spectral signatures of the two components) in the final SZ map. The resulting map used for this analysis has an angular resolution (FWHM) of 10′. We have checked that almost identical maps are obtained with other methods.

The SZ signal is clearly visible in all panels with $\log_{10}(M_*/M_\odot) \geq 11.25$. The stacked maps show no sign of a gradient in the residual signal in the vertical direction, showing that the MILCA method is very effective in removing Galactic emission. Below the mass limit of 11.25, there is also some evidence of SZ signal, although here the contrast relative to the noise is lower. Finally, we note that the signal in the lower stellar mass panels is extended. This is mainly due to the larger satellite fraction at these masses that results in a significant contribution to the stack from relatively massive halos with centres significantly offset from the locally brightest galaxy (see Figs. 2, 3 and Appendix C). We also discuss in Appendix C the impact of dust contamination on these maps.

5.2. Null tests

Null tests used to check for systematic errors are shown in Fig. 6. Taking the set of MMF filters adapted to each target galaxy, we shift their positions on the sky, either with a random displacement (i.e., by generating a random distribution of new positions isotropically distributed outside our Galactic mask) or by shifting all coordinates one degree in declination, and rerunning our analysis. In both cases the result should be zero. The shifted filter sets indeed have bin-average SZ signals consistent with zero over the entire mass range.

5.3. Size effects

Although most of the halos traced by our locally brightest galaxies are, according to their inferred R_{500} values, at most

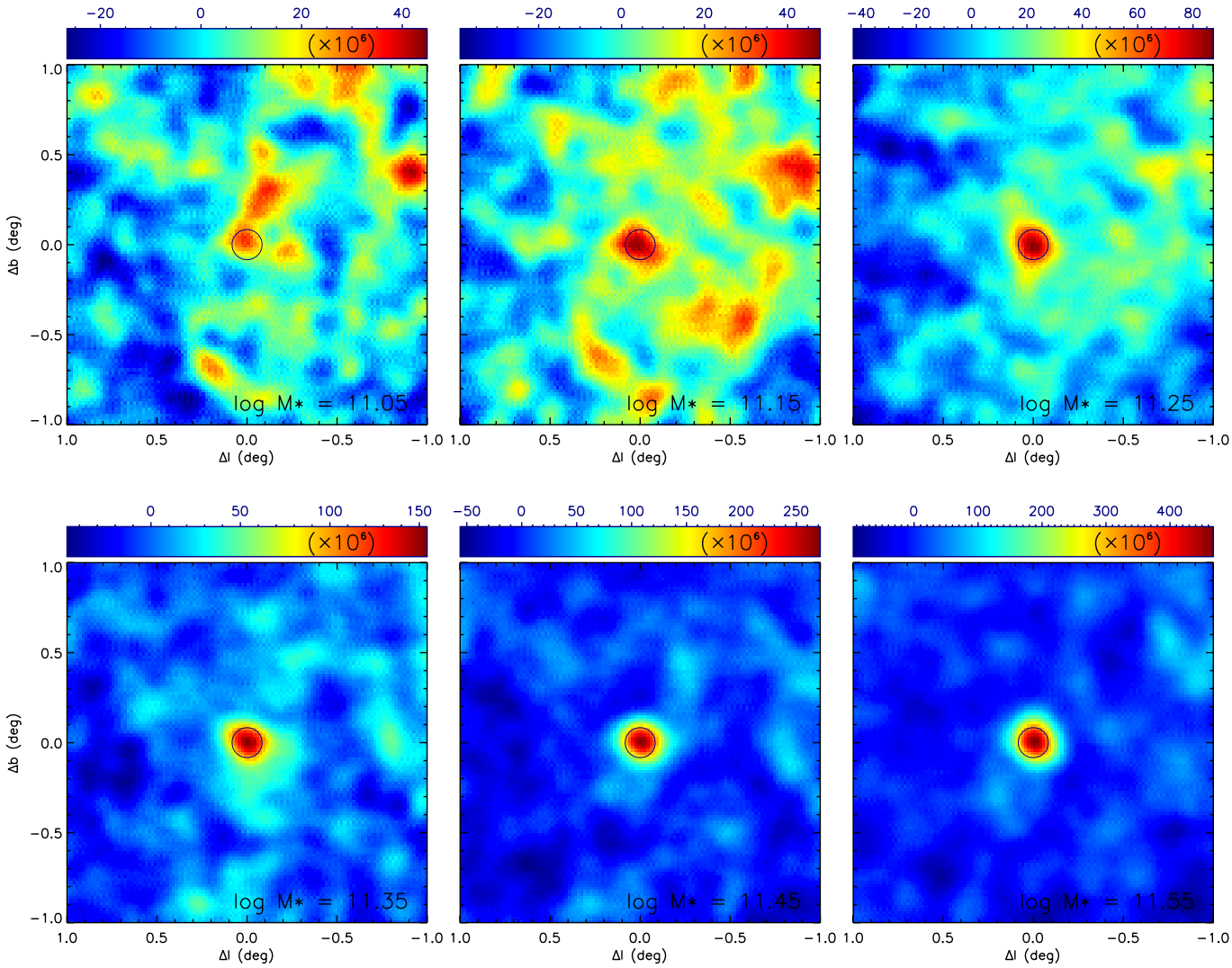

Fig. 5. Equal-weighted stacks of reconstructed SZ maps (i.e., Comptonization parameter maps) for objects in six mass bins centred, from *left to right* and *top to bottom*, at $\log_{10}(M_*/M_\odot)$ = [11.05, 11.15, 11.25, 11.35, 11.45, 11.55]. In all cases, the bin size is taken to be 0.2, so the galaxies in two consecutive panels partially overlap. Maps are 2° on a side, with Galactic north at the top. The SZ signal traced by the central galaxies is clearly detected in all bins above $\log_{10}(M_*/M_\odot) = 11.25$. In all panels, the circles indicate the FWHM of the data, which corresponds to 10′.

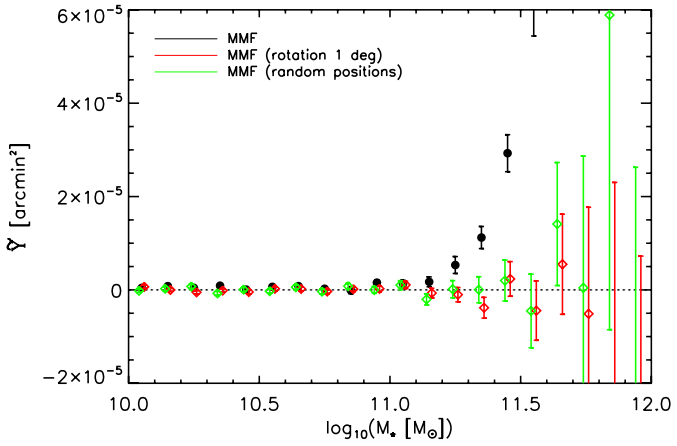

Fig. 6. Null tests performed on the locally brightest galaxy sample. Red points correspond to placing the filter one degree in declination away from the position of each LBG, while green points correspond to random high latitude filter positions. Both sets are consistent with zero. The black points show our measurements with filters centred on the LBG sample, demonstrating highly significant detections.

marginally resolved by the *Planck* beams, size effects are not negligible, and the full pressure profile has to be used for the flux determination. If instead the objects are (incorrectly) assumed to be point-like, we find that the flux is underestimated by roughly 20–30%, although the slope of the $\tilde{Y}_{500}$-M_* scaling relation is practically unaffected.

5.4. Photometry comparison

Figure 7 compares the SZ signal extracted for our LBG sample by the two photometry methods described above, namely MMF and AP. Here, we compare the total SZ flux from MMF (computed as $\tilde{Y}_{5R_{500}}$) with the total flux recovered from the AP method, after applying the correction factors described in Sect. 3. For simplicity, we assume point-like objects for the flux extraction in this analysis. This is why the MMF data points differ from the corresponding points in Fig. 4. For the AP, we also compare the nominal four-band analysis with a three-band case to illustrate the impact of residual foregrounds on our flux estimates. When the 353 GHz channel is included, the AP flux

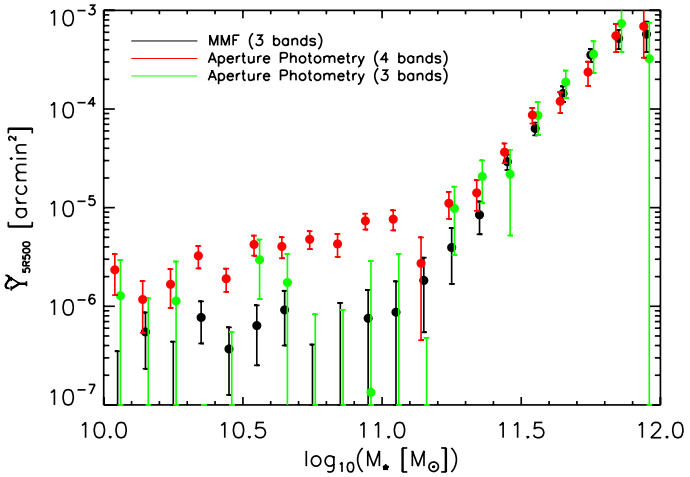

Fig. 7. Comparison of the SZ measurements on the full locally brightest galaxy sample for two different photometry methods: the matched multi-filter (MMF) and the aperture photometry (AP) approach. For this figure and only for this figure, we assume point-like objects for both methods and plot the derived total SZ flux (or the flux within $5\,R_{500}$ for MMF). The signal detected by the two methods is consistent at all stellar masses when only three frequencies are used, but when four frequencies are used, the AP results are contaminated by high frequency emission at stellar masses below $\sim 2 \times 10^{11}\ M_\odot$.

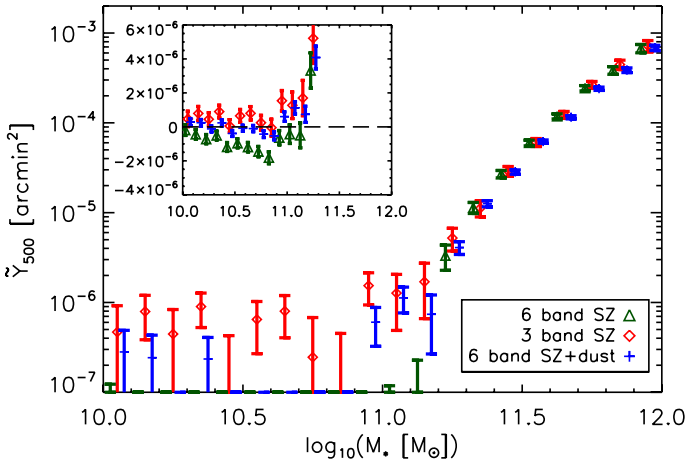

Fig. 8. Impact of dust contamination on our SZ measurements. Three cases are shown: a 6-band MMF (all *Planck* HFI frequencies) with no explicit allowance for a dust contribution (green triangles), a 3-band MMF also with no explicit dust modelling (red diamonds); and a modified 6-band MMF that includes an amplitude fit to a fiducial dust spectrum (blue crosses). The error bars include measurement uncertainties only. For stellar masses where we clearly detect the signal (i.e., at $\log_{10} M_*/M_\odot > 11.25$), the three measurements agree, indicating that dust emission does not significantly affect those measurements. At lower masses the 3-band results are consistent with the 6-band results when dust is explicitly included in the modelling, but not otherwise.

estimates at low stellar-mass are biased towards high SZ values. This indicates contaminating high-frequency emission associated with the sources, presumably dust in the LBGs or their satellites. We discuss this issue further in Sect. 5.5.

The main conclusion is that the two methods, despite their different data processing approaches, produce fully consistent results for $\log_{10}(M_*/M_\odot) \gtrsim 11.25$, while the results start to show a dependence on the method for stellar masses below that limit.

5.5. Dust contamination

The analysis of the last section suggests that our SZ signal estimates may be contaminated by residual dust emission that increases with frequency and could bias our primary results. To evaluate the potential effects, we have performed measurements using three different MMFs, as shown in Fig. 8. The green triangles and red diamonds represent the results of using all six HFI channels or only the lowest three (100, 143, 217 GHz), respectively. In both cases there is no explicit allowance for a possible dust contribution. The blue crosses show results for a modified six-band MMF that includes amplitude fits not only to the SZ spectrum, but also to a fiducial thermal dust spectrum.

The three sets of measurements fully agree for the stellar masses for which we unambiguously detect the SZ signal, $\log_{10} M_*/M_\odot \geq 11.25$. This indicates that dust emission does not significantly affect our results for these stellar mass bins. At lower mass the three-band results and the dust-corrected six-band results remain consistent, but the six-band results without explicit dust correction are systematically different. Dust emission is clearly sufficient to contaminate our six-band filter estimates of SZ signal if uncorrected, but it does not appear to be a major problem when only the lower three frequency bands are used. The residual dust contribution estimated from the scatter and offset of the red and blue points for $\log_{10} M_*/M_\odot < 11.0$ is below $\sim 10^{-6}$ arcmin^2 and so lies comfortably below our measured signal.

There is a clear indication of signal in the three bins just below $\log_{10} M_*/M_\odot = 11.25$ both for the three-band MMF and for the dust-corrected six-band MMF. However, the dust-corrected results appear systematically lower than the (uncorrected) three-band results by an amount similar to that seen at lower masses where the SZ signal is undetected. Further, the six-band MMF measurements without dust correction (the green triangles) differ substantially for these (and all lower) bins. This suggests that dust emission affects these stellar mass bins noticeably even for the three-band MMF, so the corresponding points in Fig. 4 may be more uncertain than indicated by their statistical error bars. Although formally the dust-corrected six-band MMF would appear to give our most accurate estimates of stacked SZ signal, we are uncertain whether the fiducial dust spectrum it assumes is appropriate for these specific sources. Therefore we conservatively quote results based on the three-band MMF, using the dust-corrected six-band results to give an estimate of remaining dust-related systematics.

Finally, we note that residual dust contamination biases the (uncorrected) six-band MMF signal estimates for $\log_{10} M_*/M_\odot < 11$ (Fig. 8) in the opposite direction to the AP signal estimates (see Fig. 7). The agreement of the two methods for $\log_{10} M_*/M_\odot > 11.25$ is thus a further indication of the robustness of our primary results.

5.6. Stability of the signal in different sky surveys

We have also checked that the SZ signal is stable against splitting the *Planck* data into complementary subsets. For instance, the signal obtained from the maps of the first 6 months of observing time is fully consistent with that obtained from maps of the second 6 months and the last 3.5 months (of course the latter has larger error bars due to its smaller sky coverage).

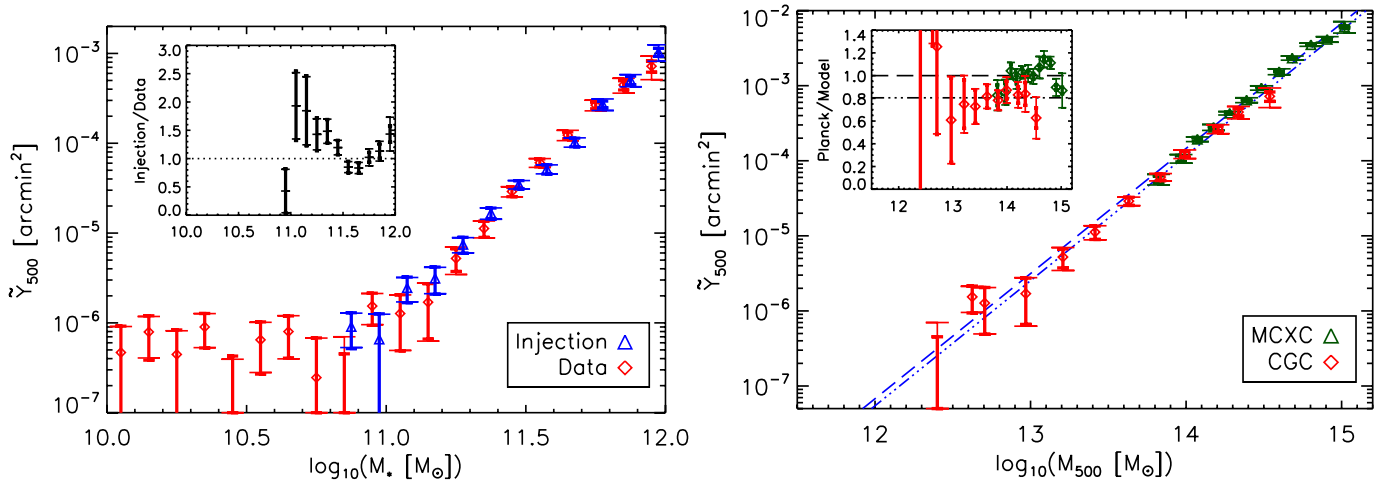

Fig. 9. *Left*: comparison of the measured mean SZ signal as a function of LBG stellar mass (red points) to simulated observations (blue points). The simulations assign to each observed LBG the halo mass and positional offset of a randomly chosen simulated LBG of the same stellar mass (compare Fig. 3). Our best fit Y_{500}-M_{500} scaling relation is then used, together with the universal pressure profile, to inject a simulated signal into the *Planck* maps (see text). An "observed" signal is obtained by applying the MMF exactly as for the real data. The inset gives the ratio of the bin-averaged injected and actual signals. *Right*: mean SZ signal as a function of effective halo mass. The bin-averaged SZ signal measurements of the left panel have been translated to this plane using the simulations as described in the text (the red points). The dot-dashed line is our best fit relation between halo mass and SZ signal, i.e., the one leading to the simulated measurements in the *left panel*. The green points give the mean SZ signal of MCXC clusters binned by a halo mass estimated from their X-ray luminosity using the REXCESS relation without correction for Malmquist bias (line 3 in Table 2 of Planck Collaboration 2011e). The dashed blue line shows the self-similar model calibrated on the REXCESS sample as given by Arnaud et al. (2010). The inset gives the ratio of all measurements to this model's predictions. As in previous figures, the thick error bars account only for measurement uncertainties, while thin bars with large terminators result from a bootstrap analysis and so include intrinsic scatter effects.

6. The Y_{500}-M_{500} relation

We now turn to the interpretation of our measurements in terms of the SZ signal-halo mass scaling relation: Y_{500}-M_{500}. Our conclusions are summarised in Fig. 9.

From our simulation of the locally brightest galaxy catalogue, we expect a large range of halo masses within a given bin of stellar mass and, in addition, a fraction of galaxies that are, in fact, satellites, with significant positional offsets relative to their host halo (see Fig. 3). These effects impact our measurements of the SZ signal-stellar mass relation in two ways. First, the MMF is not perfectly matched to each individual object because we fix the filter scale to the median halo size. This causes an aperture-induced bias in the flux measurement. Second, our filter is miscentred for those systems where the LBG is, in fact, a satellite. These galaxies are often associated with substantially more massive dark halos than typical LBGs of the same stellar mass, leading to an increase in the mean signal in the bin, mitigated by the substantial angular offsets of most such satellites from the true centres of their rich clusters. This increases the apparent extent of the signal in stacked maps like Fig. 5, but decreases the contribution to the signal through a matched filter centred on the galaxy (see Appendix C).

Using our simulation of the LBG catalogue, we can account fully for these effects and extract the underlying Y_{500}-M_{500} relation in an unbiased way. Within each stellar mass bin, we identify each observed LBG with a randomly chosen simulated LBG of the same stellar mass, assigning it the halo mass and positional offset from halo centre of its partner, but retaining its observed redshift. We give each halo a SZ signal distributed according to the "universal pressure profile" and normalized using a specific model Y_{500}-M_{500} scaling relation. Each synthesised object is then observed with the three-band MMF centred on the galaxy's position, and the measurements are binned and weighted in the same way as the real data to obtain $\langle Y \rangle_s$.

This procedure enables us to translate a model Y_{500}-M_{500} relation to our observational plane, Y_{500}-M_*, and thus to fit for the underlying scaling relation with halo mass M_{500}. We model this relation as

$$\tilde{Y}_{500} = Y_M \left(\frac{M_{500}}{3 \times 10^{14}\, M_\odot} \right)^{\alpha_M}, \quad (1)$$

fixing the mass exponent to its self-similar value, $\alpha_M = 5/3$, and fitting for the normalization Y_M. Restricting the fit to $\log_{10}(M_*/M_\odot) \gtrsim 11.5$, for direct comparison to X-ray samples in the discussion below, we find

$$Y_M = (0.73 \pm 0.07) \times 10^{-3}\ \mathrm{arcmin}^2. \quad (2)$$

In the left-hand panel of Fig. 9, the red points reproduce the measurements given in Fig. 4, while the blue points show the simulated observations for this best-fit Y_{500}-M_{500} scaling relation.

The best-fit is, however, formally unacceptable, with a reduced χ^2_ν of 3, which we can more readily appreciate from the inset showing the ratio of the actual observations to the simulated bin averages on a linear scale. The data prefer a shallower slope than the self-similar $\alpha_M = 5/3$ over the mass range of the fit. Moreover, we see that a power law cannot fit the data over the full mass range probed by our measurements. To ease comparison with the X-ray sample, we will nevertheless adopt this fit below.

The right-hand panel of Fig. 9 considers the SZ signal-halo mass plane. The blue dot-dashed line simply traces our best-fit Y_{500}-M_{500} relation. The blue dashed line is the self-similar relation derived from X-ray cluster studies in the mass range 10^{14}–10^{15} $M_\odot$ (Arnaud et al. 2010), while the green points present binned SZ measurements for the approximately 1600 clusters in the Meta-Catalogue of X-ray detected Clusters (MCXC) (Piffaretti et al. 2011). The latter measurements are

as reported in Planck Collaboration (2011e), with one minor change: in Planck Collaboration (2011e) we used an empirical slope for the Y_{500}-M_{500} relation taken from X-ray studies; for the points in Fig. 9, we repeated the same analysis fixing the slope instead to its self-similar value, as was done for the LBG sample. This change moves the green points only very slightly relative to those shown in Planck Collaboration (2011e). For the mass estimates of the MCXC objects, we applied the X-ray luminosity-mass relation from Pratt et al. (2009), corresponding to the case of line 3 of Table 2 in Planck Collaboration (2011e). The mass is calculated for each MCXC cluster and then binned. We plot the point at the median value of the mass in each bin.

To transcribe our central galaxy catalogue measurements onto this figure, we must first find the effective halo mass corresponding to each stellar mass bin. This effective mass is a complicated average over the halo masses within the bin, weighting by the fraction of SZ signal actually observed, i.e., after accounting for aperture and miscentering effects. The bin-averaged mean SZ signals we estimate for our mock LBG catalogue include all these effects, and so can be used to calculate an effective mass as $M_{500}^{\rm eff} = 3\times10^{14}\ M_\odot\ (\langle Y\rangle_{\rm s}/Y_{\rm M})^{1/\alpha_{\rm M}}$, where $\langle Y\rangle_{\rm s}$ is calculated for each bin as described above, and $Y_{\rm M}$ and $\alpha_{\rm M} = 5/3$ are the parameters used for Eq. 1 in the simulation. (Note that the result is independent of the normalisation $Y_{\rm M}$.) We do this for a suite of simulated catalogues and take the ensemble average effective mass for each bin, plotting the results as the red points in the right-hand panel of the figure.

These LBG results extend the SZ-halo mass scaling relation down in mass by at least a factor of 3, to $M_{500} = 2\times10^{13}\ M_\odot$ (the stellar mass bin at $\log_{10} M_*/M_\odot = 11.25$). This is the lowest halo mass for which the mean SZ signal has been measured. As previously discussed, there is a clear indication that the relation continues to even lower mass, with marginally significant detections in the next three stellar mass bins. The lowest stellar mass bin with an apparent SZ detection (at 2.6σ) corresponds to effective halo mass $\log_{10} M_{500}/M_\odot = 12.6$. Our power-law fit adequately describes the data points over more than two orders of magnitude in halo mass down to this remarkably low value with no hint of a significant deviation.

The inset in the right panel of Fig. 9 shows the ratio of our measured mean SZ signal to that predicted by the self-similar scaling relation deduced from X-ray observations of clusters (the dashed blue line, Arnaud et al. 2010). Direct measurements obtained by binning the MCXC clusters (the green points) agree with this relation. This was the principal result of Planck Collaboration (2011e). The SZ measurements for our LBGs fall below the relation, however. The horizontal dot-dashed line gives the ratio our LBG fit to the X-ray model (this is the offset between the two blue lines in the main figure). Recall that the fit to the LBG catalogue was restricted to masses overlapping the X-ray sample, $\log_{10} M_{500}/M_\odot > 13.8$. Over this range, the mean SZ signals associated with LBG halos are about 20% lower than found for X-ray clusters with the same halo mass, a difference that is significant at the 2.6σ level.

A number of effects could contribute to an offset of this size. The masses plotted for the MCXC were calculated using a luminosity-mass relation derived from the REXCESS sample assuming that halo mass scales self-similarly with the mass-proxy Y_X and without correction for Malmquist bias (Pratt et al. 2009). Using the Malmquist-corrected relation would remove much of the offset and bring the two Y_{500}-M_{500} scaling relations into acceptable agreement. In this sense, the offset is consistent with the estimated effects of Malmquist bias on the X-ray sample. However, such biases depend on the detailed selection procedure of the stacked and calibrating cluster samples, on the way in which the calibration relation is derived, and on the (correlated) intrinsic scatter of clusters around the L_x-M_{500} and Y_{500}-M_{500} relations. Thus they can only be corrected through detailed modelling both of the cluster population itself and of the definition and analysis of the specific cluster surveys involved (e.g., Angulo et al. 2012). Furthermore, halo masses are estimated in very different ways in our two samples – from X-ray luminosities calibrated against individual hydrostatic mass measurements for the MCXC, and through an abundance matching argument based on the WMAP7 cosmology for the LBG catalogue. Any offset between these two halo mass scales will result in offsets in Fig. 9. For example, a number of recent papers have argued that failure of some of the assumptions underlying the standard methods for estimating cluster masses from X-ray data (e.g., detailed hydrostatic equilibrium or the unimportance of turbulent and nonthermal pressure) could produce a systematic bias in the X-ray cluster mass scale (Planck Collaboration 2011g; Rozo et al. 2012; Sehgal et al. 2013). Finally, as for the LBG sample, each luminosity bin of the MCXC contains a distribution of halo properties that are averaged in complicated fashion by our stacked SZ measurement. Understanding the relative importance of these various effects at a precision better than 20% would again require detailed modeling of the heterogeneous MCXC catalogue.

7. Conclusions

Using *Planck* data, we have measured the scaling relation between Sunyaev-Zeldovich signal and stellar mass for locally brightest galaxies (Y_{500}-M_*). This is the first time such a relation has been determined, and it demonstrates the presence of hot, diffuse gas in halos hosting central galaxies of stellar mass as low as $M_* = 2\times10^{11}\ M_\odot$, with a strong indication of signal at even lower masses. We have constructed a large mock catalogue of locally brightest galaxies from the Millennium Simulation and used it to model the *Planck* observational process in detail in order to extract from our measurements the underlying SZ signal-halo mass relation (Y_{500}-M_{500}). This new relation spans a large range in halo mass, reaching from rich clusters down to $M_{500} = 2.0\times10^{13}\ M_\odot$, with a clear indication of continuation to $M_{500} \sim 4\times10^{12}\ M_\odot$. This is the lowest mass scale to which an SZ scaling relation has so far been measured. The fact that the signal is close to the self-similar prediction implies that *Planck*-detected hot gas represents roughly the mean cosmic fraction of the mass even in such low-mass systems. Consistency with their low observed X-ray luminosities then requires the gas to be less concentrated than in more massive systems. Integration of the halo mass function down to $M_{500} = 4\times10^{12} M_\odot$ shows that *Planck* has now seen about a quarter of all cosmic baryons in the form of hot gas, about four times as many as are inferred from X-ray data in clusters with $M_{500} > 10^{14} M_\odot$.

At the high mass end, the scaling relation we derive from our LBG data shows reasonable agreement with X-ray cluster results. The 20% lower normalisation that we find (significant at the 2.6σ level) can be explained in principle by a number of possible effects related to the differing selection and mass estimation methods of the two samples. Agreement at this level of precision is remarkable, and understanding the remaining difference would require detailed modeling of the selection and calibration of the X-ray samples. The fact that plausible Malmquist corrections can eliminate most of the difference shows that cluster studies are now reaching the ~10% precision level.

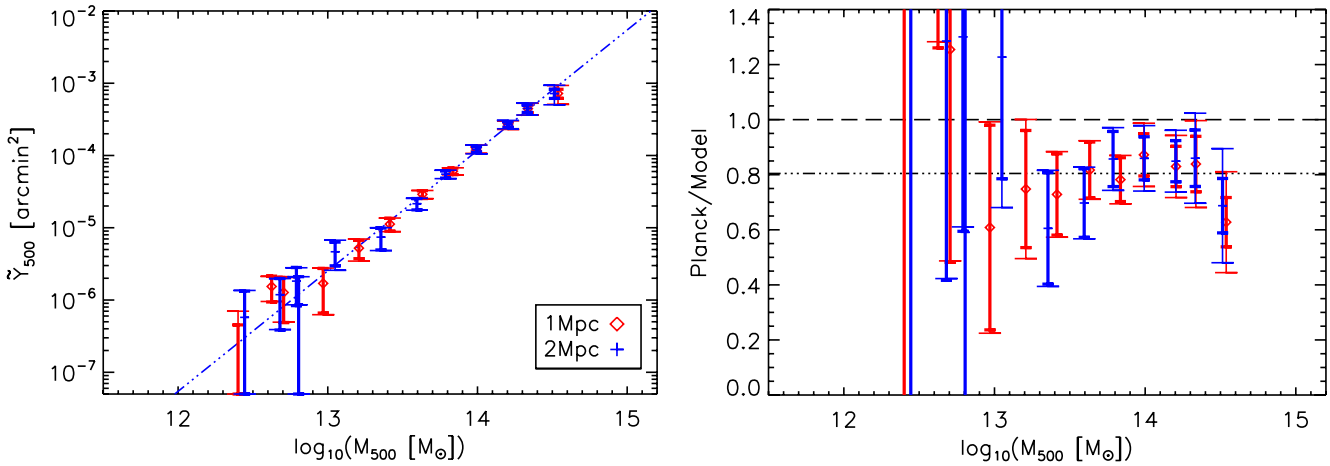

Fig. A.1. *Left*: comparison of the SZ signal-halo mass scaling relation for two different sets of isolation criteria. The triple-dot dashed line is our best fit model (see Eqs. (1) and (2)). *Right*: same as above, but now showing the ratio of the previous data points to the Arnaud et al. (2010) Y-M_{500} relation.

We find that the Y_{500}-M_{500} scaling law is described by a power law with no evidence of deviation over more than two orders of magnitude in halo mass. The gas properties of dark matter halos appear remarkably regular over a mass range where cooling and feedback processes are expected to vary strongly. In particular, we find no change in behaviour in the low-mass systems for which substantial feedback effects are invoked in current galaxy formation models (e.g., from AGN). Statistical studies of large galaxy and cluster samples, such as those presented here, can clearly shed new light on the thermal cycle at the heart of the galaxy formation process.

Acknowledgements. The authors from the consortia funded principally by CNES, CNRS, ASI, NASA, and Danish Natural Research Council acknowledge the use of the pipeline-running infrastructures Magique3 at Institut d'Astrophysique de Paris (France), CPAC at Cambridge (UK), and USPDC at IPAC (USA). The development of *Planck* has been supported by: ESA; CNES and CNRS/INSU-IN2P3-INP (France); ASI, CNR, and INAF (Italy); NASA and DoE (USA); STFC and UKSA (UK); CSIC, MICINN, JA and RES (Spain); Tekes, AoF and CSC (Finland); DLR and MPG (Germany); CSA (Canada); DTU Space (Denmark); SER/SSO (Switzerland); RCN (Norway); SFI (Ireland); FCT/MCTES (Portugal); and PRACE (EU). A description of the Planck Collaboration and a list of its members, including the technical or scientific activities in which they have been involved, can be found at `http://www.sciops.esa.int/index.php?project=planck`. We acknowledge the use of the HEALPix package (Górski et al. 2005).

Appendix A: Robustness of our results to variations in isolation criteria

As explained in Sect. 2.2, our locally brightest galaxy catalogue was built starting from a parent population with $r < 17.7$ taken from the spectroscopic NYU-VAGC and eliminating any candidate with a companion of equal or brighter r magnitude violating certain isolation criteria. In particular, we defined locally brightest galaxies to be the set of all objects with $z > 0.03$ that are brighter than all other sample galaxies projected within a radius of $R_{\rm iso} = 1.0$ Mpc, and differing in redshift by less than 1000 km s^{-1}. Hereafter, we refer to these criteria as the "1 Mpc case".

To test the robustness of our results against changes in these isolation criteria, we compared them to a case with stricter isolation criteria, $R_{\rm iso} = 2.0$ Mpc and 2,000 km s^{-1} in redshift, hereafter the "2 Mpc case".

Applying the isolation criteria to the parent spectroscopic catalogue as before, but with these new values, we end up with a first sample of 206 562 locally brightest galaxies. Again, in a second step we use SDSS photometry to further eliminate objects with companions that might violate the isolation criteria. After removing any candidate with a (photometric) companion of equal or brighter r magnitude and projected within 2.0 Mpc, we end up with a cleaned sample of 110 437 locally brightest galaxies. In particular, this sample contains 58 105 galaxies satisfying the bound $\log_{10} M_*/{\rm M}_\odot \geq 11.0$, which is the regime where we find significant SZ signal. Thus, 23 287 galaxies in this mass range are eliminated from the sample studied in the main body of this paper by the stricter isolation criteria.

To evaluate the reliability of the new $R_{\rm iso} = 2.0$ Mpc sample, we follow the same procedure as before and construct a mock sample of locally brightest galaxies from the Guo et al. (2011) simulation. As expected, the new $R_{\rm iso} = 2.0$ Mpc mock sample has a higher reliability than the $R_{\rm iso} = 1.0$ Mpc case. The fraction of locally brightest galaxies that are centrals now has a minimum of just over 87 % at stellar masses somewhat above $10^{11}\,M_\odot$. The improvement is less than might have been anticipated because, as noted in Sect. 2.2.1, the majority of the satellite galaxies in our simulated 1 Mpc sample were included because they are brighter than the central galaxies of their own halos, rather than because the isolation criteria failed to eliminate them.

Finally, Fig. A.1 compares the SZ signal-halo mass relations (Y_{500}-M_{500}) derived for the two cases (1 Mpc and 2 Mpc). Halo masses for the 2 Mpc case are computed as explained in Sect. 6 (see Table B.1 for the numerical values). The main conclusion is that the SZ signal-halo mass scaling relation is not sensitive to the isolation criteria.

Appendix B: Predicted properties of the stellar mass-halo mass relation

Using our mock catalogues based on the semi-analytic galaxy formation simulation of Guo et al. (2011), we provide here additional information on the predicted properties of the stellar mass-halo mass relation. Figure B.1 shows the distribution of

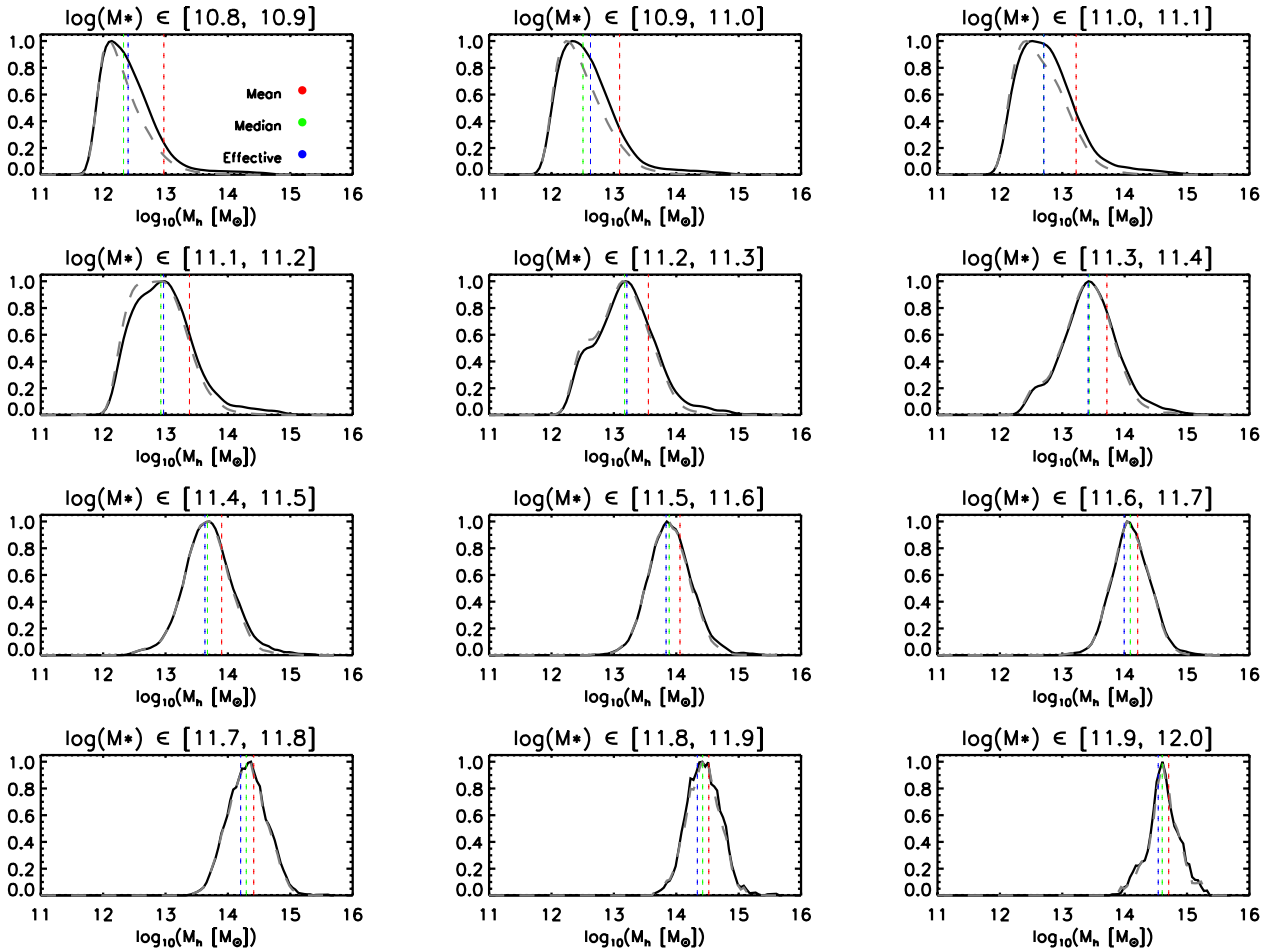

Fig. B.1. Probability distribution function of halo mass, $M_{\rm h}$, for nine of the stellar mass bins considered in this paper. Solid lines correspond to the sample isolated according to the 1 Mpc criteria, while dashed lines show the distributions for the 2 Mpc sample. Vertical colored lines show three different characteristic masses (the mean, median, and "effective" halo masses) for the 1 Mpc sample (see Table B.1 for numerical values).

Table B.1. Statistics of halo mass for various stellar mass bins, for the 1 Mpc and 2 Mpc isolation criteria.

	$\log_{10}\left(\frac{M_{\rm h}}{M_\odot}\right)$							
	$R_{\rm iso}$ = 1 Mpc				$R_{\rm iso}$ = 2 Mpc			
$\log_{10}\left(\frac{M_*}{M_\odot}\right)$	Mean	Median	RMS	Effective	Mean	Median	RMS	Effective
10.8–10.9	12.97	12.33	13.78	12.40	12.55	12.24	13.16	12.44
10.9–11.0	13.09	12.50	13.77	12.62	12.73	12.41	13.24	12.68
11.0–11.1	13.22	12.70	13.86	12.71	12.92	12.61	13.39	12.79
11.1–11.2	13.38	12.93	13.94	12.97	13.14	12.85	13.67	12.81
11.2–11.3	13.55	13.17	14.04	13.21	13.37	13.12	13.79	13.05
11.3–11.4	13.72	13.43	14.03	13.41	13.60	13.40	13.87	13.35
11.4–11.5	13.90	13.67	14.15	13.63	13.81	13.65	13.92	13.60
11.5–11.6	14.06	13.89	14.19	13.84	14.01	13.87	14.10	13.79
11.6–11.7	14.21	14.09	14.19	13.99	14.19	14.08	14.13	13.99
11.7–11.8	14.41	14.29	14.39	14.20	14.39	14.29	14.25	14.20
11.8–11.9	14.52	14.42	14.49	14.34	14.49	14.42	14.30	14.33
11.9–12.0	14.71	14.60	14.56	14.54	14.69	14.60	14.52	14.51

Notes. The first three columns for each case (mean, median, and rms values for the halo mass) are derived from the simulation only, while the effective halo mass $M_{\rm h}^{\rm eff}$ uses the redshifts and stellar masses of the observed galaxies, as described in Sect. 6. All masses (M) in this table are decimal logarithms of the value in units of $M_\odot$.

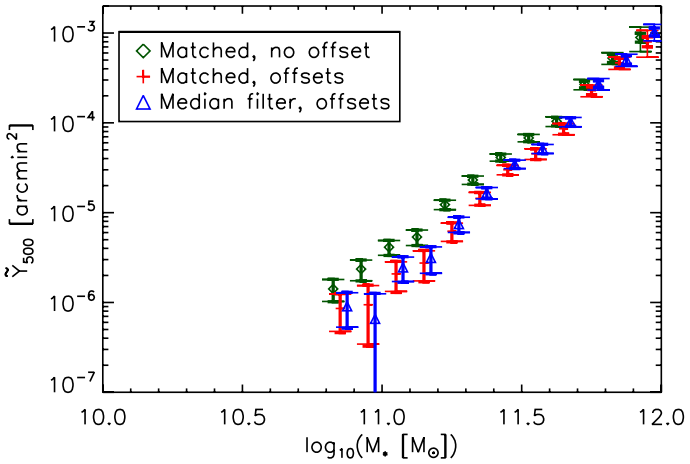

Fig. C.1. Impact of miscentering and scatter on the binned SZ measurements. The green points give results in an ideal situation with no miscentering and SZ filter perfectly matched to each individual object in a given stellar mass bin. The red crosses add the effect of miscentering, with offsets drawn from the distributions given by the simulations for each stellar mass bin. The blue triangles additionally include the aperture effect caused by fixing the filter size according to the median value of the halo mass in each bin.

halo mass (M_h) predicted for twelve of the stellar mass bins considered in this paper, and for two sets of isolation criteria: the 1 Mpc and 2 Mpc cases (see Sect. 2.2 and Appendix A). Vertical lines correspond to the mean (red), median (green), and the "effective" (blue) values of halo mass in each bin. The corresponding numbers are listed in Table B.1, which also gives the rms of the posterior M_h distribution. The effective halo masses are computed as described in Sect. 6.

Appendix C: Impact of miscentering and scatter on the binned SZ signal and stacked SZ maps

As discussed in Sec. 6, we used the semi-analytic galaxy formation simulation of Guo et al. (2011) to account for the effects of miscentering and scatter in halo mass at fixed stellar mass when interpreting our measurement (see Figs. 4 and 9). Figure C.1 isolates the impact of each effect on the binned SZ measurements, using the procedure outlined in that section. The green points represent the ideal case with no miscentering and SZ filter perfectly matched to the size of each individual object. The red crosses add miscentering offsets taken from the offset distribution in the simulations for each stellar mass bin. The drop in SZ amplitude is expected because we now miss SZ signal from the miscentered objects. Additionally fixing the filter size according to the median halo mass in each stellar mass bin, as done throughout this paper, we recover our previous results, shown as the blue triangles here and as the red diamonds in the left-hand panel of Fig. 9.

Using the same simulations, we can also estimate the impact of miscentering on the stacked SZ maps of locally brightest galaxies (see Fig. 5). Here, we use the full simulation to compute r_p, the projected distance of each locally brightest galaxy from the gravitational potential minimum of its halo. Average and RMS values for r_p for all the stellar mass bins considered in this paper and for the 1 Mpc and 2 Mpc samples are given in Table C.1. Histograms of these r_p values are shown in Fig. C.2.

Table C.1. Statistics of the distribution of distances r_p of the locally brightest galaxies from the gravitational potential minima of their parent halos, for the 1 Mpc and 2 Mpc isolation criteria.

	r_p [kpc]			
	R_{iso} = 1 Mpc		R_{iso} = 2 Mpc	
$\log_{10}\left(\frac{M_*}{M_\odot}\right)$	Mean	RMS	Mean	RMS
10.8–10.9	102.6	384.7	53.7	235.6
10.9–11.0	121.2	420.2	65.2	263.2
11.0–11.1	140.2	469.6	75.8	322.1
11.1–11.2	165.7	533.1	94.9	373.3
11.2–11.3	195.6	636.1	121.8	501.8
11.3–11.4	202.4	682.1	143.6	579.1
11.4–11.5	217.8	720.3	165.1	659.8
11.5–11.6	239.8	852.8	205.7	812.1
11.6–11.7	193.4	775.2	171.5	758.5
11.7–11.8	213.4	896.7	200.4	892.0
11.8–11.9	145.1	726.2	128.5	720.9
11.9–12.0	342.5	1062.6	332.2	1065.1

Note that the median value of r_p, which is not listed in the table, is zero for all bins.

These values can be used to predict the impact of miscentering of the locally brightest galaxy with respect to its halo (and thus, with respect to the centre of the associated SZ emission). Figure C.3 illustrates the broadening of the SZ stacked profile caused by this effect. For this computation, we assume point-like objects and a Gaussian beam profile of 10′ for easier comparison with Fig. 5. For each stellar mass bin, the M_h value from the simulation is used to predict the total SZ flux using Eqs. (1) and (2), and the r_p value is used to offset the position of the SZ signal. In order to convert r_p values (in physical units) into angular offsets, a redshift for each simulated object is drawn from the observed distribution for locally brightest galaxies of similar stellar mass. Miscentering broadens the stacked SZ profile, yielding typical FWHM of ∼20′ for $\log_{10} M_*/M_\odot \leq 11.25$, and also modifies the shape of the profile, by increasing the amount of SZ flux in the tails of the distribution. These values are slightly smaller (but comparable) to the observed widths of the SZ emission in Fig. 5.

Finally, Fig. C.4 shows equal-weighted stacks of SZ maps centred on the real central galaxy sample, similar to those of Fig. 5, but now using all six HFI frequency channels in the MILCA algorithm, rather than just the lowest four. For all six stellar mass bins the noise in these new maps, as measured by the RMS fluctuation about the mean in pixels more than 20′ from map centre, is lower than in the maps of Fig. 5. This shows that the addition of high frequency information has improved the accuracy with which non-SZ signals, primarily dust emission, are removed. Almost all this improvement comes from the inclusion of the 545 GHz channel; maps made with and without the 857 GHz channel are almost identical. As a result of this improvement, the signal-to-noise ratio of the peaks near the map centre is higher in all the panels of Fig. C.4 than in the corresponding panels of Fig. 5. This strengthens our conclusion that the apparent SZ signals near the centres of the two lowest stellar mass panels are, in fact, real, despite their apparent breadth and irregularity. The breadth is likely due to the miscentering effects explored above while the irregularity looks consistent with the overall noise level of the maps.

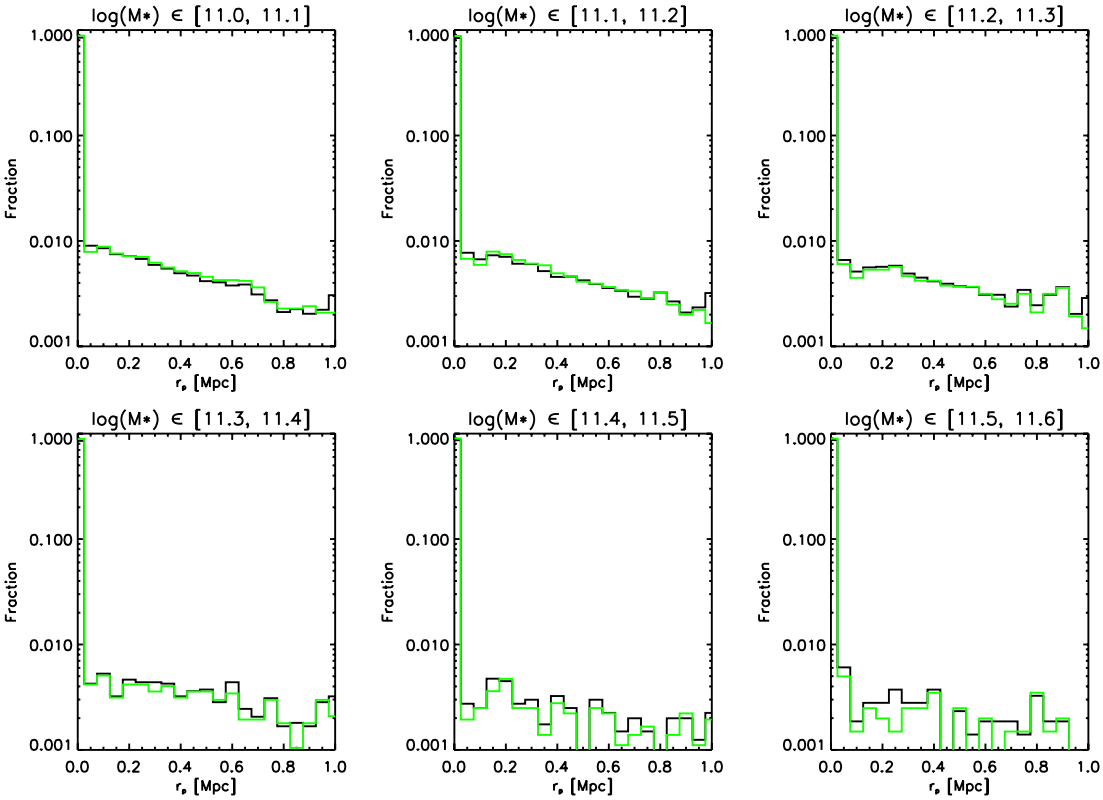

Fig. C.2. Distribution of offsets of locally brightest galaxies from the gravitational potential minima of their parent halos, both for the 1 Mpc (black) and for the 2 Mpc (green) isolation criteria. Table C.1 gives mean and rms values for these distributions.

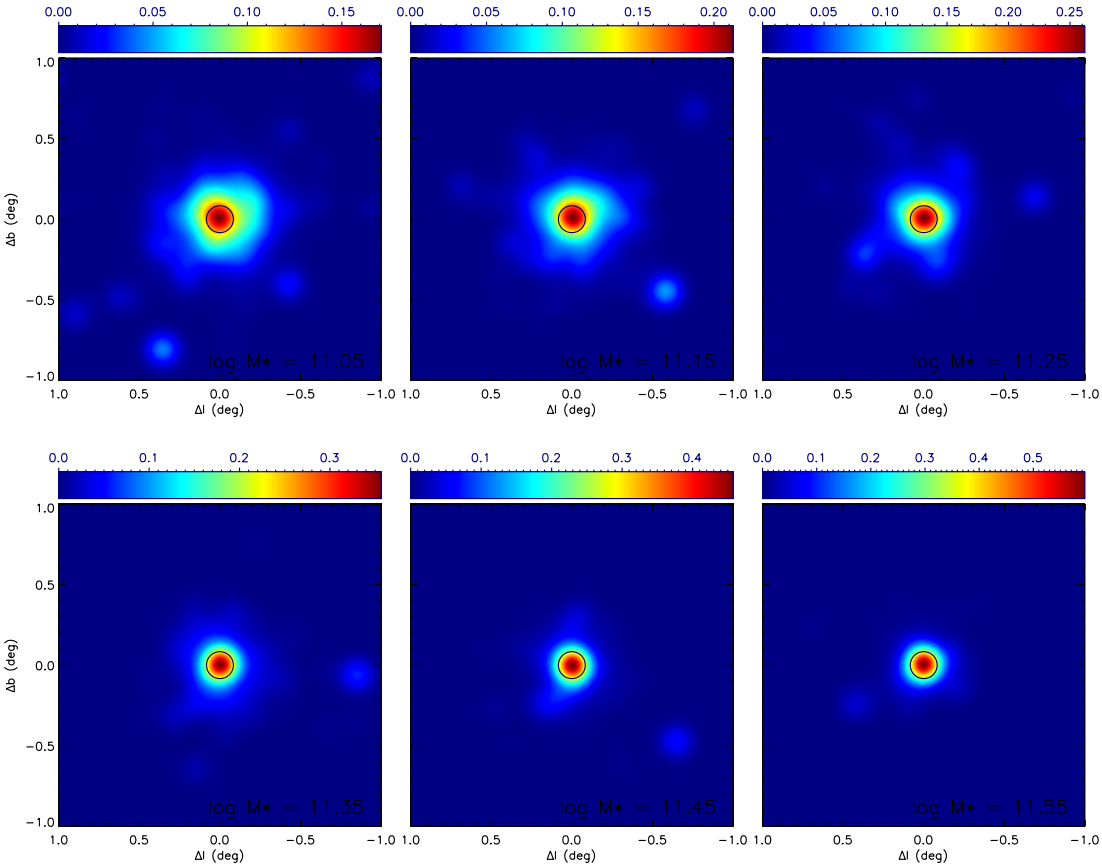

Fig. C.3. Impact of miscentering on stacked SZ maps. See the text for details of the simulation shown here. For an original resolution of $FWHM = 10'$, miscentering broadens the stacked profiles to a FWHM ~$20'$ for $\log_{10} M_*/M_\odot \leq 11.25$.

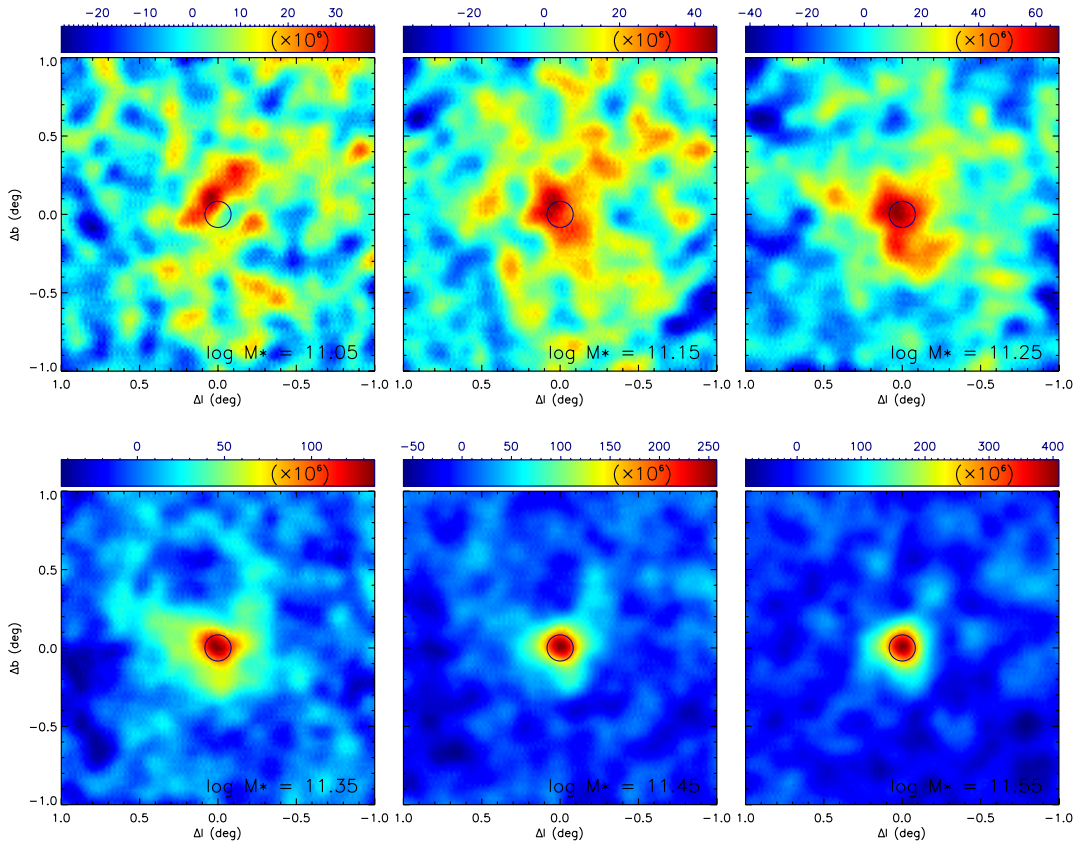

Fig. C.4. Similar to Fig. 5, but using a reconstructed SZ map that now uses all six HFI frequency channels. The noise in all maps is reduced by the inclusion of the two highest frequencies. Stacked images in the stellar-mass bins above $\log_{10}(M_*/M_\odot) = 11.25$ are not significantly affected, but for the low stellar-mass panels, the extended signal near map centre is larger and has higher signal to noise than in Fig. 5, suggesting that it may be real SZ signal broadened by miscentering effects.

References

Abazajian, K. N., Adelman-McCarthy, J. K., Agüeros, M. A., et al. 2009, ApJS, 182, 543
Angulo, R. E., & White, S. D. M. 2010, MNRAS, 405, 143
Angulo, R. E., Springel, V., White, S. D. M., et al. 2012, MNRAS, 426, 2046
Arnaud, M., Pratt, G. W., Piffaretti, R., et al. 2010, A&A, 517, A92
Balogh, M. L., Pearce, F. R., Bower, R. G., & Kay, S. T. 2001, MNRAS, 326, 1228
Bersanelli, M., Mandolesi, N., Butler, R. C., et al. 2010, A&A, 520, A4
Birkinshaw, M. 1999, Phys. Rep., 310, 97
Blanton, M. R., & Roweis, S. 2007, AJ, 133, 734
Blanton, M. R., Schlegel, D. J., Strauss, M. A., et al. 2005, AJ, 129, 2562
Blanchard, A., Valls-Gabaud, D., & Mamon, G. A. 1992, A&A, 264, 365
Böhringer, H., Schuecker, P., Pratt, G. W., et al. 2007, A&A, 469, 363
Borgani, S., Murante, G., Springel, V., et al. 2004, MNRAS, 348, 1078
Bower, R. G., Benson, A. J., Lacey, C. G., et al. 2001, MNRAS, 325, 497
Bower, R. G., Benson, A. J., Malbon, R., et al. 2006, MNRAS, 370, 645
Carlstrom, J. E., Ade, P. A. R., Aird, K. A., et al. 2011, PASP, 123, 568
Cavaliere, A., Lapi, A., & Menci, N. 2002, ApJ, 581, L1
Chabrier, G. 2003, PASP, 115, 763
Churazov, E., Sunyaev, R., Forman, W., & Böhringer, H. 2002, MNRAS, 332, 729
Cole, S. 1991, ApJ, 367, 45
Croton, D. J., Springel, V., White, S. D. M., et al. 2006, MNRAS, 365, 11
Cunha, C. E., Lima, M., Oyaizu, H., Frieman, J., & Lin, H. 2009, MNRAS, 396, 2379
Dobbs, M., Halverson, N. W., Ade, P. A. R., et al. 2006, New Astron. Rev., 50, 960
Draper, P., Dodelson, S., Hao, J., & Rozo, E. 2012, Phys. Rev. D, 85, 023005
Duffy, A. R., Schaye, J., Kay, S. T., & Dalla Vecchia, C. 2008, MNRAS, 390, L64
Eriksen, H. K., Banday, A. J., Górski, K. M., & Lilje, P. B. 2004, ApJ, 612, 633
Górski, K. M., Hivon, E., Banday, A. J., et al. 2005, ApJ, 622, 759
Guo, Q., White, S., Li, C., & Boylan-Kolchin, M. 2010, MNRAS, 404, 1111
Guo, Q., White, S., Boylan-Kolchin, M., et al. 2011, MNRAS, 413, 101
Guo, Q., White, S., Angulo, R. E., et al. 2013, MNRAS, 428, 1351
Hand, N., Appel, J. W., Battaglia, N., et al. 2011, ApJ, 736, 39
Hernández-Monteagudo, C., & Rubiño-Martín, J. A. 2004, MNRAS, 347, 403
Herranz, D., Sanz, J. L., Hobson, M. P., et al. 2002, MNRAS, 336, 1057
Hurier, G., Macias-Perez, J. F., & Hildebrandt, S. R. 2013, A&A, accepted [arXiv:1007.1149]
Koester, B. P., McKay, T. A., Annis, J., et al. 2007, ApJ, 660, 239
Komatsu, E., Smith, K. M., Dunkley, J., et al. 2011, ApJS, 192, 18
Lamarre, J., Puget, J., Ade, P. A. R., et al. 2010, A&A, 520, A9
Leahy, J. P., Bersanelli, M., D'Arcangelo, O., et al. 2010, A&A, 520, A8
Leauthaud, A., George, M. R., Behroozi, P. S., et al. 2012, ApJ, 746, 95
Lin, Y., & Mohr, J. J. 2004, ApJ, 617, 879
Mandelbaum, R., Seljak, U., Kauffmann, G., Hirata, C. M., & Brinkmann, J. 2006, MNRAS, 368, 715
Mandolesi, N., Bersanelli, M., Butler, R. C., et al. 2010, A&A, 520, A3
Marriage, T. A., Acquaviva, V., Ade, P. A. R., et al. 2011, ApJ, 737, 61
McCarthy, I. G., Schaye, J., Ponman, T. J., et al. 2010, MNRAS, 406, 822
McNamara, B. R., & Nulsen, P. E. J. 2007, ARA&A, 45, 117
Melin, J., Bartlett, J. G., & Delabrouille, J. 2006, A&A, 459, 341
Mennella, A., Butler, R. C., Curto, A., et al. 2011, A&A, 536, A3
Moster, B. P., Somerville, R. S., Maulbetsch, C., et al. 2010, ApJ, 710, 903
Navarro, J. F., Frenk, C. S., & White, S. D. M. 1997, ApJ, 490, 493
Neto, A. F., Gao, L., Bett, P., et al. 2007, MNRAS, 381, 1450
Piffaretti, R., Arnaud, M., Pratt, G. W., Pointecouteau, E., & Melin, J.-B. 2011, A&A, 534, A109
Planck Collaboration 2011a, A&A, 536, A1
Planck Collaboration 2011b, A&A, 536, A2
Planck Collaboration 2011c, A&A, 536, A8
Planck Collaboration 2011d, A&A, 536, A9
Planck Collaboration 2011e, A&A, 536, A10
Planck Collaboration 2011f, A&A, 536, A11
Planck Collaboration 2011g, A&A, 536, A12
Planck Collaboration 2012a, A&A, 550, A131
Planck Collaboration 2012b, A&A, 554, A140
Planck HFI Core Team 2011a, A&A, 536, A4
Planck HFI Core Team 2011b, A&A, 536, A6

Pratt, G. W., Croston, J. H., Arnaud, M., & Böhringer, H. 2009, A&A, 498, 361
Puchwein, E., Sijacki, D., & Springel, V. 2008, ApJ, 687, L53
Rosset, C., Tristram, M., Ponthieu, N., et al. 2010, A&A, 520, A13
Rozo, E., Bartlett, J. G., Evrard, A. E., & Rykoff, E. S. 2012 [arXiv:1204.6305]
Sehgal, N., Trac, H., Acquaviva, V., et al. 2011, ApJ, 732, 44
Sehgal, N., Addison, G., Battaglia, N., et al. 2013, ApJ, 767, 38
Somerville, R. S., Hopkins, P. F., Cox, T. J., Robertson, B. E., & Hernquist, L. 2008, MNRAS, 391, 481
Springel, V., Di Matteo, T., & Hernquist, L. 2005a, MNRAS, 361, 776
Springel, V., White, S. D. M., Jenkins, A., et al. 2005b, Nature, 435, 629
Staniszewski, Z., Ade, P. A. R., Aird, K. A., et al. 2009, ApJ, 701, 32
Sunyaev, R. A., & Zeldovich, Y. B. 1972, Comments on Astrophysics and Space Physics, 4, 173
Swetz, D. S., Ade, P. A. R., Allen, C., et al. 2008, in SPIE Conf., 7020
Tauber, J. A., Mandolesi, N., Puget, J., et al. 2010, A&A, 520, A1
Tornatore, L., Borgani, S., Springel, V., et al. 2003, MNRAS, 342, 1025
Valageas, P., & Silk, J. 1999, A&A, 350, 725
Vanderlinde, K., Crawford, T. M., de Haan, T., et al. 2010, ApJ, 722, 1180
White, S. D. M., & Frenk, C. S. 1991, ApJ, 379, 52
White, S. D. M., & Rees, M. J. 1978, MNRAS, 183, 341
Williamson, R., Benson, B. A., High, F. W., et al. 2011, ApJ, 738, 139
Zacchei, D., Maino, D., Baccigalupi, C., et al. 2011, A&A, 536, A5

[1] APC, AstroParticule et Cosmologie, Université Paris Diderot, CNRS/IN2P3, CEA/lrfu, Observatoire de Paris, Sorbonne Paris Cité, 10 rue Alice Domon et Léonie Duquet, 75205 Paris Cedex 13, France
[2] Aalto University Metsähovi Radio Observatory, Metsähovintie 114, 02540 Kylmälä, Finland
[3] Academy of Sciences of Tatarstan, Bauman Str., 20, Kazan, 420111 Republic of Tatarstan, Russia
[4] African Institute for Mathematical Sciences, 6-8 Melrose Road, Muizenberg, Cape Town, South Africa
[5] Agenzia Spaziale Italiana Science Data Center, c/o ESRIN, via Galileo Galilei, Frascati, Italy
[6] Agenzia Spaziale Italiana, Viale Liegi 26, Roma, Italy
[7] Astrophysics Group, Cavendish Laboratory, University of Cambridge, J J Thomson Avenue, Cambridge CB3 0HE, UK
[8] Atacama Large Millimeter/submillimeter Array, ALMA Santiago Central Offices, Alonso de Cordova 3107, Vitacura, Casilla 763, 0355 Santiago, Chile
[9] CITA, University of Toronto, 60 St. George St., Toronto, ON M5S 3H8, Canada
[10] CNRS, IRAP, 9 Av. colonel Roche, BP 44346, 31028 Toulouse Cedex 4, France
[11] California Institute of Technology, Pasadena, California, USA
[12] Centro de Astrofísica, Universidade do Porto, Rua das Estrelas, 4150-762 Porto, Portugal
[13] Centro de Estudios de Física del Cosmos de Aragón (CEFCA), Plaza San Juan, 1, planta 2, 44001 Teruel, Spain
[14] Computational Cosmology Center, Lawrence Berkeley National Laboratory, Berkeley, California, USA
[15] Consejo Superior de Investigaciones Científicas (CSIC), Madrid, Spain
[16] DSM/Irfu/SPP, CEA-Saclay, 91191 Gif-sur-Yvette Cedex, France
[17] DTU Space, National Space Institute, Technical University of Denmark, Elektrovej 327, 2800 Kgs. Lyngby, Denmark
[18] Département de Physique Théorique, Université de Genève, 24, Quai E. Ansermet,1211 Genève 4, Switzerland
[19] Departamento de Física Fundamental, Facultad de Ciencias, Universidad de Salamanca, 37008 Salamanca, Spain
[20] Departamento de Física, Universidad de Oviedo, Avda. Calvo Sotelo s/n, Oviedo, Spain
[21] Department of Astronomy and Geodesy, Kazan Federal University, Kremlevskaya Str., 18, 420008 Kazan, Russia
[22] Department of Astrophysics/IMAPP, Radboud University Nijmegen, PO Box 9010, 6500 GL Nijmegen, The Netherlands
[23] Department of Electrical Engineering and Computer Sciences, University of California, Berkeley, California, USA
[24] Department of Physics & Astronomy, University of British Columbia, 6224 Agricultural Road, Vancouver, British Columbia, Canada
[25] Department of Physics and Astronomy, Dana and David Dornsife College of Letter, Arts and Sciences, University of Southern California, Los Angeles, CA 90089, USA
[26] Department of Physics, Gustaf Hällströmin katu 2a, University of Helsinki, Helsinki, Finland
[27] Department of Physics, Princeton University, Princeton, New Jersey, USA
[28] Department of Physics, University of California, Berkeley, California, USA
[29] Department of Physics, University of California, Santa Barbara, California, USA
[30] Department of Physics, University of Illinois at Urbana-Champaign, 1110 West Green Street, Urbana, Illinois, USA
[31] Dipartimento di Fisica e Astronomia G. Galilei, Università degli Studi di Padova, via Marzolo 8, 35131 Padova, Italy
[32] Dipartimento di Fisica e Scienze della Terra, Università di Ferrara, via Saragat 1, 44122 Ferrara, Italy
[33] Dipartimento di Fisica, Università La Sapienza, P. le A. Moro 2, Roma, Italy
[34] Dipartimento di Fisica, Università degli Studi di Milano, via Celoria, 16, Milano, Italy
[35] Dipartimento di Fisica, Università degli Studi di Trieste, via A. Valerio 2, Trieste, Italy
[36] Dipartimento di Fisica, Università di Roma Tor Vergata, via della Ricerca Scientifica, 1, Roma, Italy
[37] Dipartimento di Matematica, Università di Roma Tor Vergata, via della Ricerca Scientifica, 1, Roma, Italy
[38] Discovery Center, Niels Bohr Institute, Blegdamsvej 17, Copenhagen, Denmark
[39] Dpto. Astrofísica, Universidad de La Laguna (ULL), 38206 La Laguna, Tenerife, Spain
[40] European Southern Observatory, ESO Vitacura, Alonso de Cordova 3107, Vitacura, Casilla 19001, Santiago, Chile
[41] European Space Agency, ESAC, Planck Science Office, Camino bajo del Castillo, s/n, Urbanización Villafranca del Castillo, Villanueva de la Cañada, Madrid, Spain
[42] European Space Agency, ESTEC, Keplerlaan 1, 2201 AZ Noordwijk, The Netherlands
[43] GEPI, Observatoire de Paris, Section de Meudon, 5 Place J. Janssen, 92195 Meudon Cedex, France
[44] Helsinki Institute of Physics, Gustaf Hällströmin katu 2, University of Helsinki, Helsinki, Finland
[45] INAF – Osservatorio Astronomico di Padova, Vicolo dell'Osservatorio 5, Padova, Italy
[46] INAF – Osservatorio Astronomico di Roma, via di Frascati 33, Monte Porzio Catone, Italy
[47] INAF – Osservatorio Astronomico di Trieste, via G.B. Tiepolo 11, Trieste, Italy
[48] INAF Istituto di Radioastronomia, via P. Gobetti 101, 40129 Bologna, Italy
[49] INAF/IASF Bologna, via Gobetti 101, Bologna, Italy
[50] INAF/IASF Milano, via E. Bassini 15, Milano, Italy
[51] INFN, Sezione di Bologna, via Irnerio 46, 40126 Bologna, Italy
[52] INFN, Sezione di Roma 1, Universit'a di Roma Sapienza, Piazzale Aldo Moro 2, 00185 Roma, Italy
[53] IUCAA, Post Bag 4, Ganeshkhind, Pune University Campus, 411 007 Pune, India
[54] Imperial College London, Astrophysics group, Blackett Laboratory, Prince Consort Road, London, SW7 2AZ, UK
[55] Infrared Processing and Analysis Center, California Institute of Technology, Pasadena, CA 91125, USA
[56] Institut Universitaire de France, 103, bd Saint-Michel, 75005 Paris, France
[57] Institut d'Astrophysique Spatiale, CNRS (UMR 8617) Université Paris-Sud 11, Bâtiment 121, Orsay, France

[58] Institut d'Astrophysique de Paris, CNRS (UMR 7095), 98 bis Boulevard Arago, 75014 Paris, France
[59] Institute for Space Sciences, Bucharest-Magurale, Romania
[60] Institute of Astro and Particle Physics, Technikerstrasse 25/8, University of Innsbruck, 6020 Innsbruck, Austria
[61] Institute of Astronomy and Astrophysics, Academia Sinica, Taipei, Taiwan
[62] Institute of Astronomy, University of Cambridge, Madingley Road, Cambridge CB3 0HA, UK
[63] Institute of Theoretical Astrophysics, University of Oslo, Blindern, Oslo, Norway
[64] Instituto de Astrofísica de Canarias, C/Vía Láctea s/n, La Laguna, Tenerife, Spain
[65] Instituto de Física de Cantabria (CSIC-Universidad de Cantabria), Avda. de los Castros s/n, Santander, Spain
[66] Jet Propulsion Laboratory, California Institute of Technology, 4800 Oak Grove Drive, Pasadena, California, USA
[67] Jodrell Bank Centre for Astrophysics, Alan Turing Building, School of Physics and Astronomy, The University of Manchester, Oxford Road, Manchester, M13 9PL, UK
[68] Kavli Institute for Cosmology Cambridge, Madingley Road, Cambridge, CB3 0HA, UK
[69] LAL, Université Paris-Sud, CNRS/IN2P3, 91405 Orsay, France
[70] LERMA, CNRS, Observatoire de Paris, 61 avenue de l'Observatoire, Paris, France
[71] Laboratoire AIM, IRFU/Service d'Astrophysique – CEA/DSM – CNRS – Université Paris Diderot, Bât. 709, CEA-Saclay, 91191 Gif-sur-Yvette Cedex, France
[72] Laboratoire de Physique Subatomique et de Cosmologie, Université Joseph Fourier Grenoble I, CNRS/IN2P3, Institut National Polytechnique de Grenoble, 53 rue des Martyrs, 38026 Grenoble Cedex, France
[73] Laboratoire de Physique Théorique, Université Paris-Sud 11 & CNRS, Bâtiment 210, 91405 Orsay, France
[74] Lawrence Berkeley National Laboratory, Berkeley, California, USA
[75] Max-Planck-Institut für Astrophysik, Karl-Schwarzschild-Str. 1, 85741 Garching, Germany
[76] Max-Planck-Institut für Extraterrestrische Physik, Giessenbachstraße, 85748 Garching, Germany
[77] National University of Ireland, Department of Experimental Physics, Maynooth, Co. Kildare, Ireland
[78] Niels Bohr Institute, Blegdamsvej 17, Copenhagen, Denmark
[79] Observational Cosmology, Mail Stop 367-17, California Institute of Technology, Pasadena, CA, 91125, USA
[80] Optical Science Laboratory, University College London, Gower Street, London, UK
[81] SISSA, Astrophysics Sector, via Bonomea 265, 34136 Trieste, Italy
[82] School of Physics and Astronomy, Cardiff University, Queens Buildings, The Parade, Cardiff, CF24 3AA, UK
[83] Space Research Institute (IKI), Profsoyuznaya 84/32, Moscow, Russia
[84] Space Sciences Laboratory, University of California, Berkeley, California, USA
[85] Special Astrophysical Observatory, Russian Academy of Sciences, Nizhnij Arkhyz, Zelenchukskiy region, 369167 Karachai-Cherkessian Republic, Russia
[86] Stanford University, Dept of Physics, Varian Physics Bldg, 382 via Pueblo Mall, Stanford, California, USA
[87] TÜBİTAK National Observatory, Akdeniz University Campus, 07058 Antalya, Turkey
[88] UPMC Univ Paris 06, UMR 7095, 98bis Boulevard Arago, 75014 Paris, France
[89] Université Denis Diderot (Paris 7), 75205 Paris Cedex 13, France
[90] Université de Toulouse, UPS-OMP, IRAP, 31028 Toulouse Cedex 4, France
[91] University Observatory, Ludwig Maximilian University of Munich, Scheinerstrasse 1, 81679 Munich, Germany
[92] University of Granada, Departamento de Física Teórica y del Cosmos, Facultad de Ciencias, Granada, Spain
[93] University of Miami, Knight Physics Building, 1320 Campo Sano Dr., Coral Gables, Florida, USA
[94] Warsaw University Observatory, Aleje Ujazdowskie 4, 00-478 Warszawa, Poland